



1 Aircraft-engine particulate matter emissions from conventional
2 and sustainable aviation fuel combustion: comparison of
3 measurement techniques for mass, number, and size

4 Joel C. Corbin^a, Tobias Schripp^b, Bruce E. Anderson^c, Greg J.
5 Smallwood^a, Patrick LeClerc^q, Ewan C. Crosbie^{c,d}, Steven Achterberg^e,
6 Philip D. Whitefield^e, Richard C. Miake-Lye^f, Zhenhong Yu^f, Andrew
7 Freedman^f, Max Trueblood^e, David Satterfield^e, Wenyan Liu^e, Patrick
8 Oßwald^b, Claire Robinson^{c,d}, Michael A. Shook^c, Richard H. Moore^c and
9 Prem Lobo^a

10 ^aMetrology Research Centre, National Research Council Canada, Ottawa, Ontario,
11 Canada

12 ^bGerman Aerospace Center (DLR), Institute of Combustion Technology, Stuttgart,
13 Germany

14 ^cNASA Langley Research Center, Hampton, Virginia, USA

15 ^dScience Systems and Applications, Inc., Hampton Virginia, USA

16 ^eDepartment of Chemistry, Missouri University of Science and Technology, Rolla,
17 Missouri, USA

18 ^fAerodyne Research, Inc., Billerica, Massachusetts, USA

19 Correspondence to: Joel C. Corbin(Joel.Corbin@nrc-cnrc.gc.ca) and Prem Lobo
20 (Prem.Lobo@nrc-cnrc.gc.ca)



21 0 AMT Feature: short summary (max. 500 characters incl. spaces)

22 The combustion of sustainable aviation fuels in aircraft engines produces
23 particulate matter (PM) emissions with different properties than conventional
24 fuels due to changes in fuel composition. Consequently, the response of various
25 diagnostic instruments to PM emissions may be impacted. We found no significant
26 instrument biases in terms of particle mass, number, and size measurements for
27 conventional and sustainable aviation fuel blends despite large differences in the
28 magnitude of emissions.

29 1 Abstract

30 Sustainable aviation fuels (SAFs) have different compositions compared to
31 conventional petroleum jet fuels, particularly in terms of fuel sulphur and
32 hydrocarbon content. These differences may change the amount and
33 physicochemical properties of volatile and non-volatile particulate matter (nvPM)
34 emitted by aircraft engines. In this study, we evaluate whether comparable nvPM
35 measurement techniques respond similarly to nvPM produced by three blends of
36 SAFs compared to three conventional fuels. Multiple SAF blends and conventional
37 (Jet A-1) jet fuels were combusted in a V2527-A5 engine, while an additional
38 conventional fuel (JP-8) was combusted in a CFM56-2C1 engine.

39 We evaluated nvPM mass concentration measured by three real-time sampling
40 techniques: photoacoustic spectroscopy, laser-induced incandescence, and the
41 extinction-minus-scattering technique. Various commercial instruments were
42 tested including three LII 300s, one PAX, one MSS+, and two CAPS PM_{SSA}. Mass-
43 based emission indices (EI_m) reported by these techniques were similar, falling
44 within 30% of their geometric mean for EI_m above 100 mg/kg_{fuel} (approximately
45 10 µg PM m⁻³ at the instrument), this geometric mean was therefore used as a
46 reference value. Additionally, two integrative measurement techniques were
47 evaluated: filter photometry and particle size distribution (PSD) integration. The
48 commercial instruments used were one TAP, one PSAP, and two SMPSSs. These
49 techniques are used in specific applications, such as on-board research aircraft to
50 determine PM emissions at cruise. EI_m reported by the alternative techniques fell
51 within approximately 50 % of the mean aerosol-phase EI_m.



52 In addition, we measured PM-number-based emissions indices using PSDs and
53 condensation particle counters. The commercial instruments used included TSI
54 SMPs, a Cambustion DMS500, and an AVL APC, and the data also fell within
55 approximately 50 % of their geometric mean. The number-based emission indices
56 were highly sensitive to the accuracy of the sampling-line penetration functions
57 applied as corrections. In contrast, the EI_m data were less sensitive to those
58 corrections since a smaller volume fraction fell within the size range where
59 corrections were substantial. A separate, dedicated experiment also showed that
60 the operating laser fluence used in the LII 300 laser-induced incandescence
61 instrument for aircraft engine nvPM measurement is adequate for a range of SAF
62 blends investigated in this study. Overall, we conclude that all tested instruments
63 are suitable for the measurement of nvPM emissions from the combustion of SAF
64 blends in aircraft engines.

65 Keywords: non-volatile particulate matter, aircraft, emissions, sustainable
66 aviation fuels, black carbon

67 2 Introduction

68 Aircraft engine particulate matter (PM) emissions are composed of non-volatile
69 (black carbon, metal ash, oxygenated functional groups) and volatile components
70 (volatile organic compounds, nitrates, sulphates) (Gagné et al., 2021; Masiol and
71 Harrison, 2014; Petzold et al., 2011). The non-volatile particulate matter (nvPM)
72 emissions are formed in the combustor, while volatile particulate matter (vPM)
73 emissions, present in the gas phase at the engine exit, condense after emission.
74 Aircraft engines emit vPM with similar or greater orders of magnitude as nvPM,
75 especially after the vapour pressure of volatile species is lowered by oxidative
76 aging (Kiliç et al., 2018) or by cooling (Beyersdorf et al., 2014). The nvPM and vPM
77 are constituents of total PM which affects air quality, health, and climate. The
78 International Civil Aviation Organization (ICAO) has developed standards and
79 recommended practices (SARPs) for measuring the mass- and number-based
80 emissions of nvPM emitted from aircraft engines with maximum rated thrust >26.7
81 kN (ICAO, 2017). Currently, SARPs have not been established for vPM or total PM
82 (Lobo et al., 2020). The SARPs for nvPM specify standardized sampling and



83 measurement protocols (SAE, 2013, 2018; ICAO, 2017), which have been
84 extensively evaluated and validated (Lobo et al., 2015b, 2020; Kinsey et al., 2021).
85 The nvPM regulatory limits are applicable for type certification of aircraft engines,
86 but they do not address the vPM which may have substantial environmental
87 impacts.

88

89 To reduce CO₂ emissions, mitigate environmental impacts, and make the aviation
90 sector more sustainable, a significant effort is underway to develop and deploy
91 sustainable aviation fuels (SAFs). Various feedstocks and different conversion
92 pathways can be used to produce SAFs (Hileman and Stratton, 2014), which differ
93 in chemical and physical properties compared to conventional petroleum jet fuel
94 (Vozka et al., 2019), most notably by lacking aromatic and sulfur species that are
95 precursors to nvPM and vPM emissions. New SAF candidates must undergo a
96 rigorous qualification and approval process (ASTM D4054) prior to being certified
97 under the ASTM D7566 standard specification as a blending component. Currently,
98 the ASTM D7566 standard allows SAF blend ratios of up to 50% with conventional
99 fuel for drop-in fuels (Wilson et al., 2013).

100

101 The combustion of neat SAFs and blends with conventional jet fuel has been shown
102 to result in different PM emissions characteristics as a function of engine type and
103 operating condition (Beyersdorf et al., 2014; Brem et al., 2015; Corporan et al.,
104 2011; Lobo et al., 2011, 2015a, 2016; Moore et al., 2017; Schripp et al., 2018, 2019;
105 Timko et al., 2010). In addition to changes in PM mass- and number-based
106 emissions, SAF combustion results in changes to particle size distributions (PSD)
107 (Beyersdorf et al., 2014; Cain et al., 2013; Kinsey et al., 2012; Lobo et al., 2011,
108 2015a, 2016; Schripp et al., 2018; Timko et al., 2010), chemical composition (Elser
109 et al., 2019; Kinsey et al., 2012; Timko et al., 2013; Williams et al., 2012),
110 morphology (Huang and Vander Wal, 2013; Kumal et al., 2020; Liati et al., 2019),
111 hygroscopic properties (Trueblood et al., 2018), and optical properties (Elser et al.,
112 2019).

113

114 The standardized sampling and measurement protocol for aircraft engine nvPM
115 emissions was designed and validated for engine certification tests using



116 conventional jet fuel. The SARP requires that number-based nvPM emissions are
117 measured with a butanol-based condensation-nuclei counter with 10 nm 50% cut-
118 size sampling in single-particle-counting mode downstream of a diluter and
119 catalytic stripper. For mass-based nvPM emissions, the instrument must be
120 insensitive to vPM and able to meet performance specifications for repeatability,
121 zero drift, linearity, limit of detection, rise time, sampling interval, accuracy, and
122 applicability. To date, the only commercial instruments that satisfy the SARP
123 number and mass measurement system requirements, respectively, are the AVL
124 Particle Counter (APC) Advanced, and the AVL Micro Soot Sensor (MSS) and the
125 Artium Laser Induced Incandescence LII 300 instrument (LII). Limited information
126 is available on aircraft engine nvPM emissions characteristics measured with the
127 standardized system for different engine types burning SAFs and blends with
128 conventional fuel (Durand et al., 2021; Elser et al., 2019; Lobo et al., 2015a, 2016).

129
130 The standardized system components are not easily adaptable for use on aircraft
131 for measurement of cruise level nvPM emissions. Consequently, there are no
132 comparable in-flight engine-emissions data available for developing and validating
133 models that predict cruise nvPM-emissions based on engine certification data.
134 Particle size distribution measurements are also not included in the standardized
135 system, which are important for assessing the effects of fuels, operating conditions,
136 and engine technologies on the environmental impacts of PM emissions. Thus to
137 advance our understanding of aircraft engine emissions and the factors that
138 control them as well as to develop a large and consistent observational data base,
139 it is important to evaluate the relative performance of other diagnostic
140 instruments that are not prescribed in the standardized protocol but meet these
141 needs. Such instruments must be evaluated for their response to nvPM and total
142 PM emissions from aircraft engines using standardized and non-standardized
143 systems, and for measurements at the engine exit plane and downstream of the
144 engine in the near field, since these instruments are typically used with minimal
145 change to their operating parameters for a wide range of sampling conditions.

146
147



148 The observations presented in this paper were collected during the NASA/DLR-
149 Multidisciplinary Airborne Experiment (ND-MAX)/ Emission and Climate Impact
150 of Alternative Fuel (ECLIF) 2 campaign that was conducted at Ramstein Air Base,
151 Ramstein-Miesenbach, Germany in January-February 2018 (see overview by
152 (Anderson and NDMAX-Team, 2021)). The campaign included ground-based and
153 in-flight measurements of emissions from the DLR Advanced Technology Research
154 Aircraft (ATRA) A320 aircraft with V2527-A5 engines running on two
155 conventional jet fuels and three blends with SAF. The main objective of the ground-
156 based measurements was to characterize the nvPM, total PM, and hydrocarbon
157 emissions as functions of engine thrust condition and fuel composition. Several
158 identical instruments were included in the in-flight sampling aircraft (NASA DC-8)
159 and ground measurement diagnostic instrument suites to enable comparisons of
160 engine emissions during ground and airborne operations, and create a data set for
161 testing cruise emission models. The NASA DC-8 aircraft with CFM56-2C1 engines
162 was also used as an emissions source to compare various emissions diagnostic
163 instruments during the ground-based measurements.

164
165 Here we present the inter-comparison of real-time measurements of aircraft
166 engine nvPM emissions in terms of physical characteristics such as mass, number,
167 and size distributions using different diagnostic instruments and measurement
168 principles. The nvPM mass emissions were evaluated using three real-time
169 sampling techniques: photoacoustic spectroscopy, the extinction-minus-scattering
170 technique, and laser-induced incandescence (LII), and two alternative
171 measurement techniques widely used in laboratories and on-board aircraft: filter-
172 based photometry and PSD integration. We note that one of the photoacoustic
173 instruments and the LII instruments have been demonstrated to be compliant with
174 the ICAO SARP performance specifications. The PM number-based emissions were
175 measured using a condensation particle counter. The PSD characteristics
176 measured by scanning mobility particle sizers and an electrical mobility
177 spectrometer were also compared. The nvPM and total PM emissions were
178 delineated using a thermal denuder and a catalytic stripper. We also report the
179 effect of laser fluence on the laser-induced incandescence of nvPM for SAF
180 combustion as changing carbon nanostructure is known to influence particle light



181 absorption and consequently LII signals, and hence the derived nvPM mass
182 concentration. The impact of fuel composition on PM emissions will be reported
183 separately (Schripp and NDMAX-Team, 2021).

184 3 Methods

185 3.1 Engine and fuels

186 In the majority of this work, emissions were sampled from a single IAE
187 V2527-A5 starboard engine of the DLR ATRA aircraft (Airbus A320-232). The
188 engine was operated on two conventional, petroleum jet fuels, referred to as REF3
189 and REF4, and three sustainable aviation fuel blends, referred to as SAF1, SAF2,
190 and SAF3. The abbreviations for the two conventional petroleum fuels are used to
191 avoid confusion with the previous ECLIF campaign (Schripp et al., 2018).

192 A limited number of experiments were also performed with JP-8 fuel,
193 combusted in the starboard CFM56-2C1 engine (#3) of the NASA DC-8 aircraft.
194 Due to limited fuel availability, none of the other five fuels could be combusted in
195 the CFM56-2C1 engine. The properties of the six fuels are summarized in Table 1.

196 3.2 Ambient conditions

197 The measurements presented in this manuscript were performed outdoors
198 during winter in western Germany. Detailed meteorology for each test point is
199 given in the supplement. The minimum, median, and maximum temperatures were
200 2.3, 2.9, 8.3 °C, respectively. Conditions were humid (>83 % humidity) and
201 sometimes rainy. Winds ranged from 0 to 15.5 km h⁻¹ and wind direction was
202 sometimes variable. The median wind direction was south-westerly, while the
203 source aircraft was oriented facing to the east. Consequently, winds blowing
204 approximately 45° angle from the right rear of the source aircraft sometimes
205 prevented the engine emissions from reaching the sampling probe at low engine
206 thrust settings.

207



208 3.3 Emissions sampling

209 An extensive suite of aerosol and gas-phase instruments operated by the
210 members of six different institutions were deployed in two different shipping
211 containers to characterize the emissions (Table 2). The complete emission-
212 sampling setup is discussed in companion papers (Anderson and NDMAX-Team,
213 2021; Schripp and NDMAX-Team, 2021). Briefly, emissions were sampled
214 through a probe located 43 m downstream of the starboard engine of the aircraft.
215 The probe was placed in front of a blast fence located on the western side of the
216 Ramstein Air Force Base flight line, and the fence redirected the engine exhaust
217 upwards for safety. The probe was connected to a 18.5-mm ID, 20-m-long
218 electrically-conductive sampling line heated to 60 °C, that transported flow to a
219 sampling plenum maintained at 33 °C. To minimize residence time and particle
220 losses in this sampling line, a pump ensured that a total of at least 137 L min⁻¹
221 flowed through the sampling manifold at all times. Higher flows produce an
222 unacceptably large pressure drop in the primary sampling line. The majority of
223 this flow was discarded as excess.

224

225 The plenum was placed inside a modified shipping container (Container 1) behind
226 the blast fence, along with the NRC, DLR, and NASA instruments. The North
227 American Reference System (NARS) was connected to the plenum by a short
228 section of heated line to the NARS dilutor box, which was heated to 60 ± 15 °C and
229 contained a custom Dekati dilutor with a dilution ratio of approximately 4 (less
230 than the standard Dekati dilutor ratio of 8 to 14). A 25 m line heated to 60 ± 15 °C
231 transferred sample aerosols flow from the dilutor box to a second shipping
232 container (Container 2), where the MST and ARI instruments were connected in
233 parallel. The NARS components include the 25 m heated line, attached diluters and
234 MST instrument suite; the system is compliant with specifications for the
235 standardized nvPM sampling and measurement system (SAE, 2013; SAE, 2018;
236 ICAO, 2017) and whose performance has been demonstrated and evaluated in
237 previous studies (Lobo et al., 2015b, 2016, 2020). Additional instrumentation
238 installed as part of the NARS included a fast electrical mobility spectrometer
239 (Cambustion DMS500), an Aerodyne Aerosol Mass Spectrometer (results not



240 presented here), and a CAPS PM_{ss}a monitor (Aerodyne Research Inc.). The details
241 of the instruments installed inside these two containers are listed in Table 3.

242 3.3.1 Gaseous measurements

243 A suite of gaseous emissions was measured in this study, as summarized in Table
244 2. The CO₂ measurements from the NASA LI-COR 7000 were in good agreement
245 with those taken by DLR (MKS MultiGas 2030 FTIR Continuous Gas Analyzer) and
246 MST (LI-COR model 840A), but had a faster response time and were therefore used
247 as the reference for instruments in Container 1. Instruments in Container 2 used
248 the MST measurements as reference.

249 3.3.2 nvPM number and particle size distributions (PSDs)

250 nvPM number concentration was measured directly by a certification-test-
251 compliant, particle counter, APC (AVL Inc., which contains a TSI Model 3790E
252 CPC), which was part of the NARS in Container 2. PSDs were measured with two
253 technologies: scanning mobility particle sizers (SMPS, TSI Inc.) and electrical
254 mobility sizers (EMS). Two types of EMS were used; the Cambustion DMS500 (in
255 Container 2, measuring particles 10 to 1000 nm in diameter) and the TSI Engine
256 Exhaust Particle Sizer (EEPS, Container 1). However, the EEPS data were excluded
257 from this analysis due to unidentified problems with the instrument which led to
258 anomalous PSDs.

259 Two SMPSs measured nvPM PSDs. An SMPS operated by NRC measured
260 particles 10 to 278 nm in diameter downstream of a catalytic stripper (Model
261 CS015, Catalytic Instruments GmbH), which heated samples to 350 °C before
262 oxidizing gas-phase VOCs to prevent them from recondensing after exiting the
263 device. Another SMPS operated by NASA measured particles 10 to 278 nm in
264 diameter either directly or downstream of a NASA-constructed thermal denuder
265 (TD) also operated at 350 °C. The TD employs a concentric activated charcoal filter
266 downstream of the sample heater to prevent re-condensation of volatile species.
267 TDs are commonly used on-board aircraft for measuring nvPM number
268 concentration and size distributions (Clarke, 1991; Moore et al., 2017) and have
269 been shown to effectively evaporate nucleation and accumulation mode sulfate
270 and organic aerosols (Beyersdorf et al., 2014; Schripp et al., 2018).



271 3.3.3 nvPM mass measurements

272 In this study, most of the nvPM mass data were derived from light
273 absorption coefficients (units of m^{-1}), either determined in flow-through sample
274 cells (the CAPS PM_{SSA} , PAX, and MSS introduced below) or after collecting particles
275 onto a filter (the TAP and PSAP introduced below). Such absorption measurements
276 can be converted to equivalent black carbon or eBC mass concentrations (eBC,
277 units of g m^{-3} ; Petzold et al. (2013)) by dividing them by a reference mass
278 absorption cross-section (MAC, units of $\text{m}^2 \text{g}^{-1}$). The LII measurements also rely on
279 light absorption, although the measurand is not absorption but incandescence at
280 two wavelengths and is termed rBC (Petzold et al., 2013; Michelsen et al., 2014).

281 The reference MAC used to report eBC represents an assumed physical
282 property of the nvPM emitted by the engine at a given time. The extensive review
283 of Bond and Bergstrom (2006) concluded that the MAC at 550 nm of externally-
284 mixed BC from a variety of sources could be summarized as $7.5 \pm 1.2 \text{ m}^2 \text{g}^{-1}$; the
285 more recent review of in-situ measurements by (Liu et al., 2020) recommended
286 $8.0 \pm 0.7 \text{ m}^2 \text{g}^{-1}$ at 550 nm. In this study, we have used the Bond and Bergstrom
287 value of $7.5 \text{ m}^2 \text{g}^{-1}$ for consistency with earlier work and instrument software.
288 These values are assumed to vary inversely with wavelength, with an Angstrom
289 (power) exponent of 1; for example, the 660 nm CAPS PM_{SSA} monitor data were
290 processed with a MAC of $7.5 \text{ m}^2 \text{g}^{-1} \times (550 \text{ nm} / 660 \text{ nm})^1 = 6.5 \text{ m}^2 \text{g}^{-1}$.

291 One eBC technique, the CAPS PM_{SSA} monitor (Aerodyne Research Inc.; Onasch et al.,
292 2015) derives absorption coefficients as the difference between measured aerosol
293 extinction and scattering coefficients, from which eBC concentrations were
294 calculated as described above. The CAPS PM_{SSA} measures light extinction by the
295 calibration-free cavity attenuation phase shift (CAPS) technique and light
296 scattering with an integrating nephelometer. The CAPS technique measures the
297 lifetime of photons in a high-finesse optical cavity comprised of two high
298 reflectivity mirrors, from which the extinction coefficient can be calculated. An
299 integrating nephelometer captures light scattered from a section of this cavity, and
300 is calibrated using the measured extinction of small (Rayleigh regime) non-
301 absorbing particles. In this study, two CAPS PM_{SSA} were present, one operated at
302 630 nm wavelength by ARI and the other at 660 nm wavelength by NRC. The



303 scattering channel of the NRC CAPS PM_{SSA} was calibrated on-site using nebulized
304 and dried ammonium sulfate particles; the other instruments were similarly
305 calibrated prior to the campaign at the manufacturer using 200 nm ammonium
306 sulfate. For the sub-200 nm particles measured in this study, no truncation
307 corrections (Modini et al., 2021) were necessary.

308 Two other eBC instruments were based on photoacoustic spectroscopy, namely
309 the Photoacoustic Extinctionmeter (PAX, DMT Inc.; Nakayama et al., 2015) and the
310 Micro Soot Sensor (MSS; AVL GmbH; Schindler et al., 2004). In both of these
311 instruments, aerosol absorption is measured by the periodic heating of particles
312 using a modulated laser, resulting in the generation of pressure waves which are
313 amplified by an acoustic cell and detected by a microphone. The PAX was
314 calibrated using nebulized ammonium sulfate as well as graphitic nanoparticles
315 (Aquadag).

316 During on-site calibration of the PAX using graphitic Aquadag nanoparticles, the
317 PAX signals were observed to drifted slowly upwards after each baseline. We were
318 nevertheless able to obtain useful data by configuring the PAX to auto-baseline
319 every 180 seconds, and only using the first 15 seconds of measurements after each
320 baseline. After the campaign, it was found that a component of the circuit board
321 was damaged during the initial shipment. In spite of this electrical problem, the
322 PAX data do not represent outliers in the following analysis.

323 Two additional pairs of eBC instruments were deployed at the ground site and on-
324 board the NASA DC-8 that measured aerosol absorption coefficients based on filter
325 attenuation, namely a Particle Soot Absorption Photometer (PSAP, Radiance
326 Research; Bond et al., 1999) and Tricolor Absorption Photometer (TAP, Brechtel
327 Manufacturing Inc. ; Ogren et al., 2017). These instruments were designed as low-
328 cost, low-maintenance devices for monitoring aerosol optical properties in the
329 background atmosphere (i.e., at low concentrations) and have been used
330 previously in airborne and ground-based studies (Moore et al., 2017). In these
331 instruments, particles are continuously collected onto an internal filter while its
332 light attenuation is measured. The change in light attenuation over time is used to
333 calculate absorption coefficients. This calculation requires post-processing to



334 correct for filter loading effects (which do not require independent measurements)
335 and may also be corrected for light attenuation due to scattering rather than
336 absorption (which requires an independent nephelometer measurement)
337 (Virkkula, 2010). Other sources of error include nonlinearities due to size-
338 dependent penetration of particles into the filter media and the evaporation of
339 volatile species over time (Lack et al., 2014; Nakayama et al., 2010). We note that
340 the TAP automatically advances its filter when its transmission drops below 80%,
341 whereas the PSAP requires a manual filter change. The PSAP filter was therefore
342 changed manually before each set of experiments herein, to ensure that its filter
343 transmission remained above 80% during all measurements.

344 Finally, three Artium LII 300 (Artium Technologies) instruments measured rBC,
345 based on two-colour pulsed laser-induced incandescence (LII) (Snelling et al.,
346 2005). These instruments heat nvPM using a 1064 nm pulsed laser and measure
347 the resulting incandescence at two wavelength bands. From this measurement,
348 rBC temperature and mass concentrations can be calculated. One of the LII 300s
349 was a component of the NARS. Of the other two, one was dedicated to an
350 experiment where its operating conditions were varied (Section 4.6). Therefore,
351 only two LII 300s were measuring real-time nvPM mass concentration
352 simultaneously at any given time. The MSS+ and the LII 300s were calibrated by
353 reference to the elemental carbon mass (defined by thermal-optical analysis)
354 produced by a laboratory diffusion-flame combustion aerosol source using
355 measurements at three mass concentrations spanning 0.1 to 0.5 mg m⁻³ (SAE,
356 2018).

357 3.4 Data analysis

358 3.4.1 Emission index calculations

359 The raw data were analysed over comparable time intervals and cross-
360 checked by independent calculations. The general analysis proceeded as described
361 in this section. First, the time series of measured CO₂ concentrations was used as a
362 reference against which to synchronize all time series, based on rapid rises and
363 falls in the observed concentrations (measured at 1 Hz) when the engine thrust



364 condition underwent large changes (as shown at 08:00 in Figure 2). All
365 instruments were synchronized against the NASA CO₂ sensor except the
366 instruments in container 2, which was synchronized against the MST LI-COR CO₂
367 sensor, because of the additional dilution stage. The time synchronization
368 accounted for different lag times due to differences in the response times and clock
369 accuracy of each instrument.

370 Second, the CO₂ concentrations [CO₂] were baseline-subtracted and filtered as
371 follows. The CO₂ baseline ([CO₂]_b) was calculated as the mean of the CO₂
372 concentrations measured before ([CO₂]₀) and after ([CO₂]₁) each test. The
373 uncertainty in this baseline value was calculated as either ([CO₂]_b - [CO₂]₀) or
374 ([CO₂]_b - [CO₂]₁), whichever was greater.

375 Due to the prevailing crosswind mentioned above, unstable CO₂ concentrations
376 occurred during from some test points at the idle engine thrust condition. These
377 unstable conditions were identified and filtered using two separate methods. In
378 the first method, the SMPS PSDs were inspected for reproducibility. In the second
379 method, an algorithm was used to reject any test points with CO₂ uncertainties
380 greater than 50%, CO₂ signals less than a factor of ten greater than uncertainty, or
381 CO₂ signals less than 20% above baseline. We found that the first method rejected
382 all of the points rejected by the algorithm, in addition to a few additional points.
383 The analysis presented uses the first method.

384 Third, all data were arithmetically averaged over the test point periods defined in
385 Table S1. For each instrument, the averaging periods were refined by inspection of
386 the data since sampling-line residence times varied. The averaged data were
387 typically at 1 Hz sampling frequency initially, although the SMPS instruments
388 measured PSDs at 45 second intervals (NRC instrument) or 30 second intervals
389 (NASA). Emission indices (EIs) were then calculated from the averaged data
390 following (SAE, 2013):

$$EI_m = PM_m \frac{RT_m}{[CO_2](M_c + \alpha M_H)P_m} \quad (1)$$

391



$$EI_{\text{num}} = \text{PN} \times 10^6 \frac{RT_m}{[\text{CO}_2](M_c + \alpha M_H)P_m} \quad (2)$$

392

393 Where EI_m and EI_{num} are mass and number-based EIs, respectively; PM_m
394 and PN are mass and number concentrations, respectively, at standard reference
395 temperature (T_m ; 273.15 K) and pressure (P_m ; 1 atm); α is the hydrogen to carbon
396 ratio of the fuel; M_c and M_H are the molar masses of carbon and hydrogen,
397 respectively; and R is the ideal gas constant (0.082 L.atm.K⁻¹.mol⁻¹).

398 3.4.2 Loss correction

399 Particles may be lost to the walls of sampling lines or to deposits on those
400 walls. The fraction of particles penetrating a given system varies with size,
401 according to a characteristic penetration function. Four penetration functions were
402 applied in this study: 1) from the probe to the sampling plenum, 2) from the
403 plenum to the NARS, 3) within the TD, and 4) within the CS (Figure 4). Function 1
404 was measured on site as described below. Function 2 was calculated using the
405 standard loss calculation methodologies provided in SAE documents AIR6504
406 (SAE, 2017) and ARP6481 (SAE, 2019). Function 3 was experimentally determined
407 in the laboratory by NASA. Function 4 was obtained from theoretical estimates and
408 experimental measurements (Catalytic Stripper manual, 2014).

409

410 Penetration function 1 (probe-to-plenum penetration) was measured
411 experimentally by nebulizing ammonium sulfate particles at the probe while all
412 instruments were sampling and all heated lines had reached thermal equilibrium.
413 (Function 1 therefore also includes the smaller instrument sampling lines
414 downstream of the plenum in its correction as well; however, these were
415 considered negligible relative to the longer probe-to-plenum and plenum-to-
416 Container-2 transport lengths.) For this measurement, the NRC SMPS was moved
417 to the probe, while the NASA instrument remained in its standard position. The
418 ratio of the NASA to NRC PSDs then provided a first estimate of the penetration
419 function. However, this first estimate was not accurate, as the measurements were
420 performed on a cold day (measured as approximately 5 °C outdoors and 15 °C in
421 the instrument container) and as it does not account for performance differences



422 between the NASA and NRC SMPSs. Therefore, two corrections were made. First,
423 both measurements were corrected to standard temperature and pressure.
424 Second, differences between the two instruments were directly measured by
425 moving the NRC SMPS just outside of the sampling container (to keep it at 5 °C)
426 and connecting it to an identical sampling line as the NASA SMPS. The ratio of the
427 two measured PSDs in this setup was defined as equal to unity at all sizes, and
428 used to correct the initial penetration function. Therefore, no further correction
429 was made for sampling lines in Container 1. Losses in this additional line were
430 negligible (calculated penetrations of 0.997 at 100 nm and 0.98 at 20 nm) relative
431 to the long NARS line to Container 2 (i.e., Function 2).

432 3.5 Uncertainties

433 All reported uncertainties and error bars represent standard errors,
434 propagated through the calculation as necessary. When two independent sources
435 of uncertainty were available (for example, the standard error in the 10 second
436 averages of [CO₂] and the uncertainty in the baseline value) they were added in
437 quadrature. Our bottom-up calculations of uncertainty can be compared with the
438 spread of the data points in our EI comparisons below. This spread represents a
439 top-down uncertainty, and is similar in magnitude to the bottom-up uncertainties
440 (i.e. error bars). This similarity lends confidence to our uncertainty estimates. In
441 most figures, error bars have generally been omitted for clarity, but uncertainties
442 are given for each instrument at each test point in Table S1.

443 4 Results and discussion

444 4.1 Experiment overview

445 A typical time series obtained when the emissions from the IAE V2527-A5 engine
446 were sampled is shown in Figure 2. Nominal low-pressure turbine fan speeds (N1)
447 expressed as a percentage of maximum continuous thrust, are shown by the labels
448 at the top of the figure. Percent N1 (along with engine fuel flow rate) is another
449 metric for representing the different engine thrust conditions and is used as a
450 primary independent variable in this study. The CO₂ concentrations (red line) were
451 highly variable at N1 = 23% as the ambient wind shifted the aircraft exhaust plume



452 toward and away from the sampling probe. Correspondingly, both nvPM mass and
453 PSD measurements were highly variable, as shown by the blue trace and black
454 symbols, respectively.

455

456 As shown in Figure 3a, nvPM mass concentrations, represented by EI_m , increased
457 with increasing N1 before decreasing slightly at the highest N1, similar to the
458 trends for other engine types reported by Lobo et al. (2015b, 2020). Figure 3b
459 shows that the relationship for EI_{num} is less clear, with a slight increase at
460 moderate N1 followed by a greater decrease at high N1. As discussed below
461 (Section 4.2.3), the higher EI_m at higher N1 thrust was associated with larger
462 particle sizes, and therefore smaller penetration-function corrections (Section
463 4.2.1). An effect of fuel composition is evident, and discussed in detail in Schripp et
464 al. (Schripp and NDMAX-Team, 2021).

465 4.2 Size distributions and penetration functions

466 4.2.1 Penetration function

467 A typical PSD, and corresponding PVD, are shown in Figure 4, in the context of the
468 penetration functions applied in this work. The PVD was calculated by assuming
469 spherical particles, which incurs negligible error for aircraft-engine nvPM due to
470 the small diameter of particles produced by such engines (Durdina et al., 2014;
471 Saffaripour et al., 2020). For the example PSD and PVD in Figure 4 (shading), it is
472 clear that a substantial fraction of the particle number was corrected for
473 penetrations (lines) of roughly 0.5. In contrast, the larger mode of the PVD
474 corresponds to penetrations larger than 0.8 in most cases. These differences led to
475 a median number- and mass-based correction factors of 1.51 and 1.19, respectively
476 for penetration Function 1 (probe to plenum) labelled in the figure. The remaining
477 instrument-specific penetration corrections were applied according to the position
478 of each instrument in the sampling system, as specified in Table 2. The magnitude
479 of each correction is given in Table S1.

480 Figure 5 shows selected PSDs from the IAE V2527-A5 engine operated with SAJF1
481 (Figure 5a) and REF4 (Figure 5b) fuels. The plot illustrates a lower (40 %) and a



482 higher thrust point (60 %) from the available data for two fuels. Note that the
483 ordinate scales are harmonized across the upper and lower rows only. All abscissa
484 scales are harmonized. The figure indicates roughly comparable PSDs from these
485 two fuels. The companion paper (Schripp and NDMAX-Team, 2021) compares the
486 effects of fuel composition in detail.

487 4.2.2 PSDs of CFM56-2C1

488 The CFM56-2C1 engine on the DC-8 burning JP-8 emitted an order of magnitude
489 more total particles per unit fuel burned than any of the fuels combusted in the
490 ATRA. We attribute this difference to the relatively high sulfur content of the JP-8
491 fuel (1490 ppm sulfur versus ≤ 105 ppm for the other fuels). The CFM56-2C1
492 engine also emitted a factor of three lower nvPM mass and nvPM number than the
493 V2527-A5 engine. The presence of extremely small particles with $d_m < 10$ nm was
494 evident in the two nvPM PSDs (not shown due to the extremely large penetration
495 function at these sizes; Figure 4). The CS-SMPS data extended to smaller diameters,
496 and showed that the size range measured by these two instruments was
497 insufficient to capture the full PSD for the CFM56-2C1 engine data at 22% N1 as
498 well as 63% N1. The $d_m < 10$ nm mode was not as prominent in the V2527-A5
499 engine exhaust at any thrust, although some evidence was observed for it (e.g.
500 number distribution at 40% N1 in Figure 5b).

501 Since the CFM56-2C1-with-JP-8 data were strongly influenced by a nucleation
502 mode, and were therefore not well described by the GMD and GSD of the data,
503 these measurements have been omitted from all subsequent PSD analysis in this
504 manuscript. Bimodal fits to the data were not possible as the nucleation mode was
505 not captured by our size distributions. However, the nvPM mass measurements
506 are much less sensitive to these small particles (Hinds, 1999) and have therefore
507 been retained. PSDs from all instruments, test points, and fuels from both the
508 CFM56-2C1 and V2527-A5 engines are included in the supplement.

509 4.2.3 Particle size statistics; GMD and GSD

510 Figure 6 summarizes the PSDs measured by three instruments in terms of their



511 GMD and GSD. The data sets labelled SMPS and TD-SMPS were both obtained from
512 NASA's SMPS, which was manually switched to a bypass line and the TD at each
513 test point. The data set labelled CS-SMPS was obtained with NRC's SMPS.

514 Total PM is represented by the data sets labelled DMS500 and SMPS. However, the
515 two are not directly comparable because the DMS500 measurements were
516 obtained after an additional dilution by a factor of 4 in the NARS and the DMS500
517 was not operated behind a volatile particle remover (CS or TD). Moreover, the
518 inversion of DMS500 data requires more assumptions about the particle size
519 distribution than the analogous SMPS calculation. Either volatiles or this inversion
520 procedure may have caused the 10% larger GSDs observed for the DMS500 for
521 some data (some measurements with GMDs over 35 nm) relative to the SMPS.
522 Since volatiles would affect both GMD and GSD, but we primarily observed
523 discrepancies in the DMS500 GSD, we suggest that the inversion was the major
524 source of bias in these data.

525
526 nvPM is represented by the open circles and filled squares in Figure 6. These two
527 data sets show a different relationship (slope) between GMD and GSD, reflecting
528 systematic differences in the corresponding PSDs. Relative to the mean of the two
529 instruments, the NRC GMDs were higher (Figure 7a) while the NRC GSDs were
530 higher at $GSD < 1.75$ but lower at $GSD > 1.75$ (Figure 7b). Inspection of the
531 corresponding PSDs showed that the NASA and NRC instruments agreed at higher
532 d_m but that NRC number concentrations were higher at smaller d_m . This trend
533 suggests that a bias in the penetration functions applied to each instrument
534 (Figure 4, Table 2) led to the discrepancy in GMD and GSD. Such a bias would affect
535 the nvPM concentration estimated from these PSDs (Figure 8b) and will be
536 discussed further below.

537 In spite of these trends in GMD and GSD, the PSD measurements agreed to within
538 20% (Figure 7a) for nvPM GMDs and within 5% for nvPM GSDs (Figure 7b).
539 Furthermore, these measurements are consistent with previous measurements by
540 Lobo et al. (2015c), as illustrated by the line in Figure 6, which reproduces the
541 polynomial best-fit line reported by those authors.



542 4.3 Consistency between number-based emission indices of nvPM and
543 vPM

544 Figure 7c compares the measured vPM and nvPM $E_{I_{num}}$ with the mean nvPM $E_{I_{num}}$
545 (i.e., mean of the NRC CS-SMPS, NASA TD-SMPS, and NARS APC. The grey shading
546 shows that all instruments agreed to within a factor of 2. The APC and DMS500
547 nvPM $E_{I_{num}}$ were both typically higher than the two similar SMPSs. The APC has a
548 50% efficiency at its cut-off diameter of 10 nm, reaching 100% efficiency above
549 this size and 0% below it. Therefore, relative to the SMPSs, which measured down
550 to approximately 10 nm with 100% efficiency, the APC should measure lower than
551 the SMPSs since it will underperform at sizes close to 10 nm. (This expectation
552 requires that there are no particles present above the SMPS upper detection limit
553 of 280 nm in our study, which was verified by our PSD analysis in Section 3 and
554 Table 2). However, the APC measured approximately 50% larger nvPM $E_{I_{num}}$
555 under all conditions, and our measured PSDs rule out the possibility that 50% of
556 particles were not seen by the SMPS. Therefore, we attribute the difference
557 between APC and SMPS results to uncertainties in the APC or SMPS penetration
558 correction functions. Since the two SMPSs agreed, the APC measurements were
559 likely overcorrected when the SARP correction procedures were applied.

560 We also attribute the larger nvPM $E_{I_{num}}$ measured by the DMS500 to the same
561 cause; to which a similar penetration function as the APC applies (Section 3.4.2).

562 4.4 Consistency between mass-based emission indices

563 4.4.1 E_{I_m} measurements by real-time sampling instruments

564 Figure 8a presents scatterplots of the real-time E_{I_m} measurements acquired during
565 this study for all fuels and both engine types. In Figure 8a, the individual E_{I_m} are
566 plotted against the geometric mean of the instruments shown in the caption: three
567 LII 300 instruments, two CAPS instruments, one PAX and one MSS+. The geometric
568 mean was chosen over the more-common arithmetic mean because the data are
569 not normally distributed; the arithmetic mean would therefore have over-
570 emphasized outliers.



571 Figure 9a presents the same data as Figure 8a except that the measurements have
572 been normalized to the geometric-mean EI_m from Figure 8a. Most data fall within
573 30 % of the mean (inner dashed lines) above $100 \text{ mg} / \text{kg}_{\text{fuel}}$. We note that exhaust
574 samples were diluted with background air by a factor of 40 or more before
575 reaching the inlet probe, so at this lower limit, the actual concentration observed
576 by the instruments was approximately $10 \mu\text{g m}^{-3}$ (the exact conversion factor
577 varies with CO_2 concentration and fuel properties), which is close to their
578 detection limits, as expected. This lower limit may have been influenced by the
579 ambient measurement conditions, where background nvPM concentrations were
580 non-negligible.

581 The agreement of the real-time measurements to within 30 % is notable
582 considering the different types of instruments used. The scatter at lower EI_m
583 values reflects the noise levels of the instruments. Both of these observations are
584 consistent with data reported previously for different engine types by Lobo et al.
585 (2016, 2020). The LII 300 and MSS+ from the North American Reference System
586 (NARS) have been widely used to characterize aircraft engine nvPM emissions. The
587 two CAPS instruments were independently calibrated and operated. The MSS+ and
588 PAX represent two photoacoustic spectrometers from different manufacturers,
589 operated by different teams, with different principles of calibration. The PAX was
590 also operated with a damaged capacitor on its printed circuit board. As noted in
591 Methods, these instruments operate on a variety of physical principles, including
592 photoacoustic spectroscopy (with two different designs), extinction-minus-
593 scattering, and laser-induced incandescence (cf. Section 3.3.3). Agreement
594 between these various principles also suggests that factors such as volatile
595 coatings on nvPM did not influence the instrument responses.

596 4.4.2 SMPS-based EI_m

597 Figure 8b and Figure 9b are analogous to Figure 8a and Figure 9a, but for the
598 integrative nvPM measurements that do not fall into the real-time sampling
599 category. These data are plotted against the same geometric mean from Figure 8a.
600 The dashed lines in Figure 9b represent the same ratios as in Figure 9a.
601 Considering that the real-time instruments in Figure 8a were either calibrated to



602 aerosol absorption or to aviation nvPM, we consider their accuracy as greater than
603 the instruments in Figure 8b and consider departures from the 1:1 line as due to
604 inaccuracy.

605 Most of the instruments in Figure 8b were accurate to within 30% of the reference,
606 similar to Figure 8a, with the exception of the CS-SMPS and PSAP. This is
607 summarized in Table 3, which shows the mean ratios of all data except engine idle
608 (23% N1) with the geometric mean. Table 3 also includes the results of a linear
609 regression against the geometric mean to facilitate comparison of our
610 measurements with Kinsey et al. (2021), who performed linear regressions against
611 simultaneous elemental carbon (EC) measurements (in our study, mass
612 concentrations were too low to obtain EC measurements). The PSAP data are
613 discussed in the next section. The CS-SMPS data were systematically higher than
614 the geometric mean, potentially due to an overcorrection of the penetration of
615 large particles to the SMPS.

616 Since the spread of nvPM EI_m reported by the two SMPS systems was smaller than
617 the bias, their difference relative to the reference EI_m cannot be attributed to
618 measurement imprecision. Since the two SMPS systems showed different
619 accuracies, their differences cannot be ascribed to a lack of constraints on the
620 effective density of the nvPM particles (Momenimovahed and Olfert, 2015), which
621 may vary with the monomer diameter (Abegglen et al., 2014; Durdina et al., 2014)
622 and/or shape of soot aggregates. With respect to the real-time measurements, the
623 TD-SMPS data are also consistent with previous measurements of aviation engine
624 PSDs, which, however, were not corrected for diffusional particle loss (Lobo et al.,
625 2015b, 2020). Careful measurement of the penetration functions used in these
626 calculations would be required to confirm our interpretation.

627 4.4.3 Filter photometer-based EI_m from TAP and PSAP

628 Figure 8b and Figure 9b show that the TAP measurements were within the 30 %
629 range observed for the real-time instruments, with a relative standard deviation
630 (RSD) of 14 % (Table 3) for all data excluding the engine idle condition (23% N1).
631 This provides high confidence for the use of the TAP for in-flight or field



632 measurements of aircraft-engine nvPM mass emissions, when filter-loading
633 corrections (Section 3.3.3) are correctly applied.

634 The PSAP, on the other hand, showed much greater variability, with an RSD of 36%
635 (Table 3). This is substantially higher than the variability reported by a laboratory
636 intercomparison of PSAP and CAPS PM_{SSA} (Perim De Faria et al., 2021) (that study
637 did not report a statistic comparable to RSD). Although the PSAP has been
638 observed to deviate up to a factor of two higher in cases of high organic aerosol
639 loading or reduced filter transmission (Lack et al., 2013), our data are restricted to
640 transmissions above 0.8. The fact that the PSAP shows great variability rather than
641 a fixed offset indicates that the issue is not due to a systematic error such as an
642 inaccurate MAC or flow rate calibration. We note that the TAP and PSAP were
643 operated with reduced sample flow rates of 0.05 L min⁻¹ and 0.1 L min⁻¹,
644 respectively, (5 to 10% of nominal settings) to extend the life of their filter media
645 while sampling the high soot concentrations in the aircraft exhaust. Under these
646 conditions, detector noise and small fluctuations in sample flow have a magnified
647 effect on resulting derived absorption coefficients. We suspect that the
648 measurements would have been significantly more precise if the instruments had
649 been operated at nominal flows, although this would have required changing
650 filters after each test point. Consistent with our hypothesis, we note that
651 Nakayama et al. (2010) observed substantially larger variability in PSAP
652 measurements at 0.3 than at 0.7 standard litres per minute. We also note that Bond
653 et al. (1999) did not observe an impact of flow rate when changing from 1 to 2
654 litres per minute.

655 Figure 10 plots as a function of particle GMD the same relative TAP and PSAP EI_m
656 data shown in Figure 9b. No clear trend of this ratio with size is evident, although
657 the measurements become somewhat more scattered at smaller sizes for the SAF1
658 data set, where signal to noise is lower (GMD and EI_m were correlated, see the
659 below discussion of Figure 12). Figure 10b includes the size-dependent PSAP
660 correction function reported by Nakayama et al. (2010) (their Equation 8), with
661 shading representing a 1σ uncertainty. Those authors predicted the true
662 absorption values using Mie theory for nigrosin particles of diameter 100 to
663 600 nm and refractive index 1.685–0.285*i*. Thus, their correction factor is



664 conceptually equivalent to our $E_{I_m}/\text{mean-}E_{I_m}$. Extrapolating their correction
665 function down from 100 nm to 15 nm gives values ranging from 4 to 8, whereas
666 our measurements are close to 1.0. This discrepancy may be attributed primarily
667 to the extrapolation, and possibly also to the fact that we have measured solid
668 nvPM particles rather than liquid nigrosin. Overall, it is clear that the variability in
669 our PSAP data is not sufficiently predicted by the GMD.

670 Overall, our data show that any possible size dependency in the TAP and PSAP
671 response is smaller than the observed variability between samples. The TAP and
672 PSAP data exhibit relative standard deviations (RSD) of 19% and 16%,
673 respectively, for samples with GMD > 25 nm. Future studies may consider
674 correcting PSAP and TAP measurements by the ratios shown in Table 3, which
675 represent the ratio between the calibrated aerosol-phase nvPM mass
676 measurements and the previously uncalibrated PSAP and TAP measurements, for
677 data above 25 mg $\text{kg}_{\text{fuel}}^{-1}$ and $N_1 > 40\%$.

678 4.5 Instrument performance for fuels with different composition

679 Figure 11 shows a category plot of the ratio $E_{I_m}/\text{mean-}E_{I_m}$ (that is, the ordinate of
680 Figure 9) for the different instruments. Data below 100 mg / kg_{fuel} have been
681 excluded as this ratio reflects only noise in that region (Figure 9). The symbols
682 have been sized by mean N_1 . The data have been coded by symbol and colour to
683 reflect the 6 fuels used in this study, although JP-8 measurements are few in
684 number due to the E_{I_m} of the data set (CFM56-2C1 with JP-8) being typically below
685 25 mg / kg_{fuel} .

686 Figure 11 shows that no substantial difference can be seen for these instruments
687 for the nvPM E_{I_m} for fuels with different composition; the spread in the data for a
688 given fuel is larger than the difference between fuels. Outliers tend to be associated
689 with low N_1 (small symbols). Because low N_1 corresponds to both lower
690 concentrations (lower signal-to-noise) and lower exhaust velocities relative to
691 ambient wind speeds, these outliers are not surprising.

692 The instruments in Figure 11 show a linear response to nvPM mass and operate on
693 a range of physical principles. This observation indicates that no instrument was



694 uniquely sensitive to changes in particle size over the observed range, since EI_m
695 was correlated with GMD (Figure 12), as is typical of aviation engines (Saffaripour
696 et al., 2020). We note that the response of all of these instruments is proportional
697 to the MAC of the sample, so that it remains possible that the sample MAC changed
698 with GMD or EI_m .

699 4.6 Influence of LII laser fluence

700 An additional experiment was performed to test the hypothesis that the laser
701 fluence of the LII 300 may not be sufficiently high to heat nvPM to incandescence
702 in aircraft-engine PM emissions from SAFs at different engine thrusts. This
703 hypothesis is related to electron microscopy evidence (Vander Wal et al., 2014)
704 showing that the degree of graphitization of aircraft-engine soot may be
705 substantially lowered at low thrusts. A lower degree of graphitization may result in
706 a lower LII signal if the 1064 nm MAC is lower (resulting in a lower maximum
707 temperature being reached) or if part of the laser energy leads to carbon annealing
708 rather than thermal excitation (Botero et al., 2021; Ugarte, 1992; Vander Wal and
709 Choi, 1999). If correct, this hypothesis would mean that the nvPM concentrations
710 reported by an LII 300 operated at reduced fluence would be lower than those of a
711 reference LII 300. Higher fluences are also required for nvPM internally mixed
712 with volatile PM, as some laser energy may be lost to volatile evaporation
713 (Michelsen et al., 2015).

714 Figure 13a illustrates the experiment we performed to test this hypothesis. The
715 figure presents data for SAF1 only; results for other fuels were similar. One
716 “reduced-fluence” LII 300 was programmed to change its Q-switch delay from
717 140 μs to 240 μs , with a randomized order. In this experiment, lower Q-switch
718 delays corresponded to higher laser fluence; the lowest Q-switch delay was the
719 optimal one for this system. Another “reference” LII 300 operated with no change
720 to its Q-switch delay. Figure 13a shows that the reduced-fluence LII reported lower
721 mass concentrations when its Q-switch delay was increased, but returned to the
722 expected values when its Q-switch delay was reduced.

723 We defined R_{LII} as the ratio of nvPM mass concentrations reported by the reduced-



724 fluence and reference LII 300 instruments. Figure 13b shows that R_{LII} was a
725 function of Q-switch delay, and therefore laser fluence, for all engine thrust
726 conditions. This observation is expected, since LII signals are lower at lower
727 fluence (Michelsen et al., 2015) and since we calculated R_{LII} without taking this
728 effect into account. We have verified in our laboratory that Q-switch delay is
729 inversely proportional to laser fluence for this system and that saturation effects
730 are negligible.

731 A trend of decreasing R_{LII} with decreasing N1 is evident at moderate and low Q-
732 switch delays, which can be interpreted as indicating that the nvPM was more
733 graphitic at higher N1 conditions. However, R_{LII} reached a plateau at high fluence
734 (smaller Q-switch delay), which is the region where the LII 300 normally operates.
735 This plateau was reached at all engine thrusts, with a broader range for the plateau
736 at higher thrusts and a decreasing range as the thrust was lowered. Therefore, the
737 LII 300 has sufficient fluence and can be expected to perform well for SAF blends
738 at all engine thrust conditions.

739 5 Conclusions

740 For multiple instruments measuring nvPM number, size, and mass, we observed
741 no evidence of anomalous instrument responses to the exhaust emissions
742 produced by SAF blends relative to reference fuels (REFs) combustion in an IAE
743 V2527-A5 engine. The GMD, GSD, and EI_{num} data for all fuels fell within 20%, 5%,
744 and a factor of 2 of their mean, respectively. Anomalous instrumental responses
745 would have resulted in two groups of data for these parameters, which was not
746 observed. However, a difference between EI_{num} for instruments located on
747 different-length sampling lines was noted and attributed to a greater sensitivity of
748 EI_{num} than EI_m to the penetration function.

749
750 The majority of nvPM mass measurements by the real-time instruments (CAPS
751 PM_{SSA} , LII 300, MSS+, PAX) agreed to within 30% of their geometric mean
752 (reference mean), for EI_m above 100 mg/kg_{fuel}. This lower limit corresponded to a
753 mass concentration of approximately 10 $\mu\text{g m}^{-3}$ (the conversion of EI_m to mass
754 varies because the emitted $[\text{CO}_2]$ varies), which was the noise level of these



755 instruments. The ratio of each real-time measurement with the reference mean
756 was close to unity (maximally 1.24, minimally 0.78) and indicated good precision
757 (all RSDs $\leq 17\%$).

758

759 Integrative nvPM EI_m , calculated from PSD measurements or filter attenuation
760 (TAP and PSAP), fell within a factor of two of the reference mean. The ratio of each
761 integrative measurement with the reference mean was further from unity
762 (maximally 1.50, minimally 0.88) and variability was higher precision (all RSDs
763 $\leq 36\%$). The variability in TAP data was notably low at 14%, and the variability in
764 PSAP data was notably high at 36%, likely due to its operation at a reduced flow
765 rate.

766

767 Two other instrument- and fuel composition-specific observations were made. A
768 dedicated experiment showed that changing the laser fluence of an LII 300 could
769 influence its reported nvPM mass concentrations at low to moderate fluences. By
770 maintaining sufficiently high fluence a plateau region was established, irrespective
771 of thrust or fuel, where reported nvPM mass concentrations were stable and not
772 influenced by experimental conditions. Second, additional measurements of
773 emissions from JP-8 fuel combusted in a CFM56-2C1 engine indicated the presence
774 of very high concentrations of volatile nucleation-mode particles with
775 diameter < 20 nm. These measurements reflect a different engine, as well as a fuel
776 with a factor 20 higher sulfur content, and the increased total PM number
777 concentration is most likely attributable to the sulfur.

778

779 Overall, this study found that real-time instruments for the measurement of nvPM
780 emissions in aviation turbine engines are comparable whether conventional fuels
781 or SAFs are used. Since all real-time measurements were influenced by the MAC
782 and no independent measurement of nvPM mass was made, no conclusions about
783 the variability thereof can be made from this study.



784 5.1 Author contributions

785 BEA, PLC, TS, PL, GJS, PDW, and RML designed the study. JCC, TS, PLC, GJS, ECC, SA,
786 PDW, RML, ZY, AF, MT, DS, WL, CR, PO, MS, and PL took the measurements. JCC, TS,
787 BEA, RHM, MAS, ECC, SA, ZY analyzed the data with input from GJS, PL, RML, and
788 AF. JCC prepared the figures. JCC and PL drafted the manuscript. All authors
789 discussed the data interpretation and presentation.

790 5.2 Competing interests

791 RML and AF are employed by ARI, which produces the CAPS PM_{SSA} commercially.
792 ZY was employed by ARI at the time of the study.

793 5.3 Acknowledgements

794 We acknowledge the efforts of the flight and ground crews of the DLR ATRA, the
795 NASA DC8, and the U.S. Air Force 86th Air Wing. We thank the ground staff of
796 Ramstein Air Base for their operational support during this experiment.

797 5.4 Financial support

798 This research received funding from the Transport Canada project “TC Aviation —
799 nvPM from renewable and conventional fuels”. The campaign was funded by the
800 DLR aeronautics program in the framework of the project “Emission and Climate
801 Impact of Alternative Fuels (ECLIF)”. MS&T and ARI received support from the U.S.
802 Federal Aviation Administration (FAA) through the Aviation Sustainability Center
803 (ASCENT) – a U.S. FAA-NASA- U.S. DoD-Transport Canada- U.S. EPA sponsored
804 Center of Excellence for Alternative Jet Fuels and Environment under Grant No. 13-
805 C-AJFE-MST, Amendment 010. A.F. was supported by funds from ARI. ATRA
806 operational and fuel costs along with DLR scientists’ participation was funded by
807 the DLR aeronautics program in the framework of the project “Emission and
808 Climate Impact of Alternative Fuels (ECLIF)”. The U.S. FAA Office of Environment
809 and Energy and the National Aeronautics and Space Administration Aeronautics
810 Research Mission Directorate supported field and DC-8 operations, and
811 participation of the U.S. researchers in the project.



812 5.5 Data availability

813 The data presented in Figures 4 to 10 are available in the Zenodo repository at
814 <https://sandbox.zenodo.org/record/950512> as a spreadsheet file. Other data are
815 available from the authors upon request.

816 6 References

- 817 ASTM D4054: Practice for Evaluation of New Aviation Turbine Fuels and Fuel Additives.
818 Conshohocken, PA: ASTM International; 2019. doi: 10.1520/D4054-19.
- 819 ASTM D7566: Specification for Aviation Turbine Fuel Containing Synthesized
820 Hydrocarbons. Conshokocken, PA: ASTM International; 2020. doi: 10.1520/D7566-20
- 821 International Civil Aviation Organization (2017). International Standards and
822 Recommended Practices – Annex 16 to the Convention on International Civil Aviation:
823 Environmental Protection, Volume II - Aircraft Engine Emissions, 4th ed., Montreal, QC,
824 Canada.
- 825 Abegglen, M., Durdina, L., Mensah, A., Brem, B., Corbin, J., Wang, J., Lohmann, U. and Sierau,
826 B.: Effective density measurements of fresh particulate matter emitted by an aircraft
827 engine, in EGU General Assembly Conference Abstracts, vol. 16, p. 14367., 2014.
- 828 Anderson, B. E. and NDMAX-Team: Overview of the NASA/DLR Multidisciplinary Airborne
829 Experiment (ND-MAX), in prep., 2021.
- 830 ASTM D4054: Practice for Evaluation of New Aviation Turbine Fuels and Fuel Additives.
831 Conshohocken, PA: ASTM International; 2019. doi: 10.1520/D4054-19.
- 832 ASTM D7566: Specification for Aviation Turbine Fuel Containing Synthesized
833 Hydrocarbons. Conshokocken, PA: ASTM International; 2020. doi: 10.1520/D7566-20
- 834 Beyersdorf, A. J., Timko, M. T., Ziemba, L. D., Bulzan, D., Corporan, E., Herndon, S. C.,
835 Howard, R., Miake-Lye, R., Thornhill, K. L., Winstead, E., Wey, C., Yu, Z. and Anderson, B. E.:
836 Reductions in aircraft particulate emissions due to the use of Fischer-Tropsch fuels,
837 *Atmos. Chem. Phys.*, 14(1), 11–23, doi:10.5194/acp-14-11-2014.
- 838 Bond, T. C. and Bergstrom, R. W.: Light absorption by carbonaceous particles: An
839 investigative review, *Aerosol Sci. Technol.*, 40(1), 27–67,
840 doi:10.1080/02786820500421521, 2006.
- 841 Bond, T. C., Anderson, T. L. and Campbell, D.: Calibration and Intercomparison of Filter-
842 Based Measurements of Visible Light Absorption by Aerosols, *Aerosol Sci. Technol.*, 30(6),
843 582–600, doi:10.1080/027868299304435, 1999.
- 844 Botero, M. L., Akroyd, J., Chen, D., Kraft, M. and Agudelo, J. R.: On the thermophoretic
845 sampling and TEM-based characterisation of soot particles in flames, *Carbon N. Y.*, 171,
846 711–722, doi:10.1016/j.carbon.2020.09.074, 2021.
- 847 Brem, B. T., Durdina, L., Siegerist, F., Beyerle, P., Bruderer, K., Rindlisbacher, T., Rocci-
848 Denis, S., Andac, M. G., Zelina, J., Penanhoat, O. and Wang, J.: Effects of Fuel Aromatic
849 Content on Nonvolatile Particulate Emissions of an In-Production Aircraft Gas Turbine,
850 *Environ. Sci. Technol.*, 49(22), 13149–13157, doi:10.1021/acs.est.5b04167, 2015.
- 851 Cain, J., Dewitt, M. J., Blunck, D., Corporan, E., Striebich, R., Anneken, D., Klingshirn, C.,
852 Roquemore, W. M. and Vander Wal, R.: Characterization of gaseous and particulate
853 emissions from a turboshaft engine burning conventional, alternative, and surrogate fuels,



- 854 Energy Fuels, 27(4), 2290–2302, doi:10.1021/ef400009c, 2013.
- 855 Catalytic Stripper CS015 Instrument Manual, Catalytic Instruments GmbH, 2014.
- 856 Clarke, A. D.: A thermo-optic technique for in situ analysis of size-resolved aerosol
857 physicochemistry, *Atmos. Environ. Part A, Gen. Top.*, 25(3–4), 635–644,
858 doi:10.1016/0960-1686(91)90061-B, 1991.
- 859 Corporan, E., Edwards, T., Shafer, L., Dewitt, M. J., Klingshirn, C., Zabarnick, S., West, Z.,
860 Striebich, R., Graham, J. and Klein, J.: Chemical, thermal stability, seal swell, and emissions
861 studies of alternative jet fuels, *Energy Fuels*, 25(3), 955–966, doi:10.1021/ef101520v,
862 2011.
- 863 Durand, E., Lobo, P., Crayford, A., Sevcenco, Y. and Christie, S.: Impact of fuel hydrogen
864 content on non-volatile particulate matter emitted from an aircraft auxiliary power unit
865 measured with standardised reference systems, *Fuel*, 287, 119637,
866 doi:10.1016/j.fuel.2020.119637, 2021.
- 867 Durdina, L., Brem, B. T., Abegglen, M., Lobo, P., Rindlisbacher, T., Thomson, K. A.,
868 Smallwood, G. J., Hagen, D. E., Sierau, B. and Wang, J.: Determination of PM mass emissions
869 from an aircraft turbine engine using particle effective density, *Atmos. Environ.*, 99, 500–
870 507, doi:10.1016/j.atmosenv.2014.10.018, 2014.
- 871 Elser, M., Brem, B. T., Durdina, L., Schönenberger, D., Siegerist, F., Fischer, A. and Wang, J.:
872 Chemical composition and radiative properties of nascent particulate matter emitted by
873 an aircraft turbofan burning conventional and alternative fuels, *Atmos. Chem. Phys.*,
874 19(10), 6809–6820, doi:10.5194/acp-19-6809-2019, 2019.
- 875 Gagné, S., Couillard, M., Gajdosechova, Z., Momenimovahed, A., Smallwood, G., Mester, Z.,
876 Thomson, K., Lobo, P. and Corbin, J. C.: Ash-Decorated and Ash-Painted Soot from Residual
877 and Distillate-Fuel Combustion in Four Marine Engines and One Aviation Engine, *Environ.*
878 *Sci. Technol.*, 55, 6584–6593, doi:10.1021/acs.est.0c07130, 2021.
- 879 Hileman, J. I. and Stratton, R. W.: Alternative jet fuel feasibility, *Transp. Policy*, 34, 52–62,
880 doi:10.1016/j.tranpol.2014.02.018, 2014.
- 881 Hinds, W. C.: *Aerosol technology: properties, behavior, and measurement of airborne*
882 *particles*, John Wiley & Sons., 1999.
- 883 Huang, C. H. and Vander Wal, R. L.: Effect of soot structure evolution from commercial jet
884 engine burning petroleum based JP-8 and synthetic HRJ and FT fuels, *Energy Fuels*, 27(8),
885 4946–4958, doi:10.1021/ef400576c, 2013.
- 886 ICAO: *International Standards and Recommended Practices – Annex 16 to the Convention*
887 *on International Civil Aviation: Environmental Protection, Volume II - Aircraft Engine*
888 *Emissions*, Montreal, QC., 2017.
- 889 International Civil Aviation Organization (2017). *International Standards and*
890 *Recommended Practices – Annex 16 to the Convention on International Civil Aviation:*
891 *Environmental Protection, Volume II - Aircraft Engine Emissions*, 4th ed., Montreal, QC,
892 Canada.
- 893 Kiliç, D., El Haddad, I., Brem, B. T., Bruns, E., Bozetti, C., Corbin, J., Durdina, L., Huang, R. J.,
894 Jiang, J., Klein, F., Lavi, A., Pieber, S. M., Rindlisbacher, T., Rudich, Y., Slowik, J. G., Wang, J.,
895 Baltensperger, U. and Prévôt, A. S. H.: Identification of secondary aerosol precursors
896 emitted by an aircraft turbofan, *Atmos. Chem. Phys.*, 18(10), 7379–7391, doi:10.5194/acp-
897 18-7379-2018, 2018.
- 898 Kinsey, J. S., Timko, M. T., Herndon, S. C., Wood, E. C., Yu, Z., Miake-Lye, R. C., Lobo, P.,
899 Whitefield, P., Hagen, D., Wey, C., Anderson, B. E., Beyersdorf, A. J., Hudgins, C. H., Thornhill,
900 K. L., Edward, W., Howard, R., Bulzan, D. I., Tacina, K. B. and Knighton, W. B.: Determination



- 901 of the emissions from an aircraft auxiliary power unit (APU) during the alternative
902 aviation fuel experiment (AAFEX), *J. Air Waste Manag. Assoc.*, 62(4), 420–430,
903 doi:10.1080/10473289.2012.655884, 2012.
- 904 Kinsey, J. S., Giannelli, R., Howard, R., Hoffman, B., Frazee, R., Aldridge, M., Leggett, C.,
905 Stevens, K., Kittelson, D., Silvis, W., Stevens, J., Lobo, P., Achterberg, S., Swanson, J.,
906 Thomson, K., McArthur, T., Hagen, D., Trueblood, M., Wolff, L., Liscinsky, D., Arey, R.,
907 Cerully, K., Miake-Lye, R., Onasch, T., Freedman, A., Bachalo, W., Payne, G. and Durlicki, M.:
908 Assessment of a regulatory measurement system for the determination of the non-volatile
909 particulate matter emissions from commercial aircraft engines, *J. Aerosol Sci.*, 154,
910 105734, doi:10.1016/j.jaerosci.2020.105734, 2021.
- 911 Kumal, R. R., Liu, J., Gharpure, A., Vander Wal, R. L., Kinsey, J. S., Giannelli, B., Stevens, J.,
912 Leggett, C., Howard, R., Forde, M., Zelenyuk, A., Suski, K., Payne, G., Manin, J., Bachalo, W.,
913 Frazee, R., Onasch, T. B., Freedman, A., Kittelson, D. B. and Swanson, J. J.: Impact of Biofuel
914 Blends on Black Carbon Emissions from a Gas Turbine Engine, *Energy Fuels*, 34(4), 4958–
915 4966, doi:10.1021/acs.energyfuels.0c00094, 2020.
- 916 Lack, D. A., Moosmüller, H., McMeeking, G. R., Chakrabarty, R. K. and Baumgardner, D.:
917 Characterizing elemental, equivalent black, and refractory black carbon aerosol particles:
918 a review of techniques, their limitations and uncertainties, *Anal. Bioanal. Chem.*, 406(1),
919 99–122, doi:10.1007/s00216-013-7402-3, 2014.
- 920 Liati, A., Schreiber, D., Alpert, P. A., Liao, Y., Brem, B. T., Corral Arroyo, P., Hu, J., Jonsdottir,
921 H. R., Ammann, M. and Dimopoulos Eggenschwiler, P.: Aircraft soot from conventional
922 fuels and biofuels during ground idle and climb-out conditions: Electron microscopy and
923 X-ray micro-spectroscopy, *Environ. Pollut.*, 247, 658–667,
924 doi:10.1016/j.envpol.2019.01.078, 2019.
- 925 Liu, F., Yon, J., Fuentes, A., Lobo, P., Smallwood, G. J. and Corbin, J. C.: Review of recent
926 literature on the light absorption properties of black carbon: Refractive index, mass
927 absorption cross section, and absorption function, *Aerosol Sci. Technol.*, 54(1), 33–51,
928 doi:10.1080/02786826.2019.1676878, 2020.
- 929 Lobo, P., Hagen, D. E. and Whitefield, P. D.: Comparison of PM emissions from a commercial
930 jet engine burning conventional, biomass, and fischer-tropsch fuels, *Environ. Sci. Technol.*,
931 45(24), doi:10.1021/es201902e, 2011.
- 932 Lobo, P., Christie, S., Khandelwal, B., Blakey, S. G. and Raper, D. W.: Evaluation of Non-
933 volatile Particulate Matter Emission Characteristics of an Aircraft Auxiliary Power Unit
934 with Varying Alternative Jet Fuel Blend Ratios, *Energy Fuels*, 29(11), 7705–7711,
935 doi:10.1021/acs.energyfuels.5b01758, 2015a.
- 936 Lobo, P., Durdina, L., Smallwood, G. J., Rindlisbacher, T., Siegerist, F., Black, E. A., Yu, Z.,
937 Mensah, A. A., Hagen, D. E., Miake-Lye, R. C., Thomson, K. A., Brem, B. T., Corbin, J. C.,
938 Abegglen, M., Sierau, B., Whitefield, P. D. and Wang, J.: Measurement of aircraft engine non-
939 volatile PM emissions: Results of the Aviation-Particle Regulatory Instrumentation
940 Demonstration Experiment (A-PRIDE) 4 campaign, *Aerosol Sci. Technol.*, 49(7), 472–484,
941 doi:10.1080/02786826.2015.1047012, 2015b.
- 942 Lobo, P., Hagen, D. E., Whitefield, P. D. and Raper, D.: PM emissions measurements of in-
943 service commercial aircraft engines during the Delta-Atlanta Hartsfield Study, *Atmos.*
944 *Environ.*, 104, 237–245, doi:10.1016/j.atmosenv.2015.01.020, 2015c.
- 945 Lobo, P., Condevaux, J., Yu, Z., Kuhlmann, J., Hagen, D. E., Miake-Lye, R. C., Whitefield, P. D.
946 and Raper, D. W.: Demonstration of a Regulatory Method for Aircraft Engine Nonvolatile
947 PM Emissions Measurements with Conventional and Isoparaffinic Kerosene fuels, *Energy*
948 *Fuels*, 30(9), 7770–7777, doi:10.1021/acs.energyfuels.6b01581, 2016.



- 949 Lobo, P., Durdina, L., Brem, B. T., Crayford, A. P., Johnson, M. P., Smallwood, G. J., Siegerist,
950 F., Williams, P. I., Black, E. A., Llamedo, A., Thomson, K. A., Trueblood, M. B., Yu, Z., Hagen, D.
951 E., Whitefield, P. D., Miake-Lye, R. C. and Rindlisbacher, T.: Comparison of standardized
952 sampling and measurement reference systems for aircraft engine non-volatile particulate
953 matter emissions, *J. Aerosol Sci.*, 145, 105557, doi:10.1016/j.jaerosci.2020.105557, 2020.
- 954 Masiol, M. and Harrison, R. M.: Aircraft engine exhaust emissions and other airport-related
955 contributions to ambient air pollution: A review, *Atmos. Environ.*, 95, 409–455,
956 doi:10.1016/j.atmosenv.2014.05.070, 2014.
- 957 Michelsen, H. A., Schulz, C., Smallwood, G. J. and Will, S.: Laser-induced incandescence:
958 Particulate diagnostics for combustion, atmospheric, and industrial applications, *Prog.
959 Energy Combust. Sci.*, 51, 2–48, doi:10.1016/j.pecs.2015.07.001, 2015.
- 960 Modini, R. L., Corbin, J. C., Brem, B. T., Irwin, M., Bertò, M., Pileci, R. E., Fetfatzis, P.,
961 Eleftheriadis, K., Henzing, B., Moerman, M. M., Liu, F., Müller, T. and Gysel-Beer, M.:
962 Detailed characterization of the CAPS single-scattering albedo monitor (CAPS PM_{SSA}) as a
963 field-deployable instrument for measuring aerosol light absorption with the extinction-
964 minus-scattering method, *Atmos. Meas. Tech.*, 14(2), doi:10.5194/amt-14-819-2021,
965 2021.
- 966 Momenimovahed, A. and Olfert, J. S.: Effective Density and Volatility of Particles Emitted
967 from Gasoline Direct Injection Vehicles and Implications for Particle Mass Measurement,
968 *Aerosol Sci. Technol.*, 49(11), 1051–1062, doi:10.1080/02786826.2015.1094181, 2015.
- 969 Moore, R. H., Thornhill, K. L., Weinzierl, B., Sauer, D., D’Ascoli, E., Kim, J., Lichtenstern, M.,
970 Scheibe, M., Beaton, B., Beyersdorf, A. J., Barrick, J., Bulzan, D., Corr, C. A., Crosbie, E., Jurkat,
971 T., Martin, R., Riddick, D., Shook, M., Slover, G., Voigt, C., White, R., Winstead, E., Yasky, R.,
972 Ziemba, L. D., Brown, A., Schlager, H. and Anderson, B. E.: Biofuel blending reduces particle
973 emissions from aircraft engines at cruise conditions, *Nature*, 543(7645), 411–415,
974 doi:10.1038/nature21420, 2017.
- 975 Nakayama, T., Kondo, Y., Moteki, N., Sahu, L. K., Kinase, T., Kita, K. and Matsumi, Y.: Size-
976 dependent correction factors for absorption measurements using filter-based
977 photometers: PSAP and COSMOS, *J. Aerosol Sci.*, 41(4), 333–343,
978 doi:10.1016/j.jaerosci.2010.01.004, 2010.
- 979 Nakayama, T., Suzuki, H., Kagamitani, S., Ikeda, Y., Uchiyama, A. and Matsumi, Y.:
980 Characterization of a Three Wavelength Photoacoustic Soot Spectrometer ({PASS}-3) and
981 a Photoacoustic Extinctionmeter ({PAX}), *J. Meteorol. Soc. Japan. Ser. {II}*, 93(2), 285–308,
982 doi:10.2151/jmsj.2015-016, 2015.
- 983 Ogren, J. A., Wendell, J., Andrews, E. and Sheridan, P. J.: Continuous light absorption
984 photometer for long-Term studies, *Atmos. Meas. Tech.*, 10(12), 4805–4818,
985 doi:10.5194/amt-10-4805-2017, 2017.
- 986 Onasch, T. B., Massoli, P., Keibian, P. L., Hills, F. B., Bacon, F. W. and Freedman, A.: Single
987 Scattering Albedo Monitor for Airborne Particulates, *Aerosol Sci. Technol.*, 49(4), 267–279,
988 doi:10.1080/02786826.2015.1022248, 2015.
- 989 Perim De Faria, J., Bundke, U., Freedman, A., Onasch, T. B. and Petzold, A.: Laboratory
990 validation of a compact single-scattering albedo (SSA) monitor, *Atmos. Meas. Tech.*, 14(2),
991 1635–1653, doi:10.5194/amt-14-1635-2021, 2021.
- 992 Petzold, A., Ogren, J. A., Fiebig, M., Laj, P., Li, S.-M., Baltensperger, U., Holzer-Popp, T., Kinne,
993 S., Pappalardo, G., Sugimoto, N., Wehrli, C., Wiedensohler, A. and Zhang, X.-Y.:
994 Recommendations for the interpretation of “black carbon” measurements, *Atmos. Chem.
995 Phys.*, 13(16), 8365–8379, doi:10.5194/acp-13-8365-2013, 2013.



- 996 SAE International. Aerospace Information Report (AIR) 6241 . Procedure for the
997 Continuous Sampling and Measurement of Non-Volatile Particle Emissions from Aircraft
998 Turbine Engines. Warrendale, PA, 2013. <https://doi.org/10.4271/AIR6241>
- 999 SAE international. Aerospace Recommended Practice (ARP) 6320 - Procedure for the
1000 Continuous Sampling and Measurement of Non-Volatile Particulate Matter Emissions from
1001 Aircraft Turbine Engines, Warrendale, PA, 2018. <https://doi.org/10.4271/ARP6320>.
- 1002 SAE International. Aerospace Information Report (AIR) 6504 - Procedure for the
1003 Calculation of Sampling System Penetration Functions and System Loss Correction
1004 Factors, Warrendale, PA, 2017. <https://doi.org/10.4271/AIR6504>
- 1005 SAE International. Aerospace Recommended Practice (ARP) 6481- Procedure for the
1006 Calculation of Sampling Line Penetration Functions and Line Loss Correction Factors,
1007 Warrendale, PA, 2019. <https://doi.org/10.4271/ARP6481>
- 1008 Saffaripour, M., Thomson, K. A., Smallwood, G. J. and Lobo, P.: A review on the
1009 morphological properties of non-volatile particulate matter emissions from aircraft
1010 turbine engines, *J. Aerosol Sci.*, 139, doi:10.1016/j.jaerosci.2019.105467, 2020.
- 1011 Schindler, W., Haisch, C., Beck, H. A., Niessner, R., Jacob, E. and Rothe, D.: A photoacoustic
1012 sensor system for time resolved quantification of diesel soot emissions, *SAE Technical
1013 Paper 2004-01-0968*, SAE International., doi:10.4271/2004-01-0968, 2004.
- 1014 Schripp, T. and NDMAX-Team: Aircraft Engine Particle Emissions from Sustainable
1015 Aviation Fuels: Results from Ground Measurements during the NASA/DLR Campaign
1016 ECLIF2/ND-MAX, 2021.
- 1017 Schripp, T., Anderson, B., Crosbie, E. C., Moore, R. H., Herrmann, F., Oßwald, P., Wahl, C.,
1018 Kapernaum, M., Köhler, M., Le Clercq, P., Rauch, B., Eichler, P., Mikoviny, T. and Wisthaler,
1019 A.: Impact of Alternative Jet Fuels on Engine Exhaust Composition during the 2015 ECLIF
1020 Ground-Based Measurements Campaign, *Environ. Sci. Technol.*, 52(8), 4969–4978,
1021 doi:10.1021/acs.est.7b06244, 2018.
- 1022 Schripp, T., Herrmann, F., Oßwald, P., Köhler, M., Zschocke, A., Weigelt, D., Mroch, M. and
1023 Werner-Spatz, C.: Particle emissions of two unblended alternative jet fuels in a full scale jet
1024 engine, *Fuel*, 256, 115903, doi:10.1016/j.fuel.2019.115903, 2019.
- 1025 Snelling, D. R., Smallwood, G. J., Liu, F., Gülder, Ö. L. and Bachalo, W. D.: A calibration-
1026 independent laser-induced incandescence technique for soot measurement by detecting
1027 absolute light intensity, *Appl. Opt.*, 44(31), 6773, doi:10.1364/ao.44.006773, 2005.
- 1028 Timko, M. T., Yu, Z., Onasch, T. B., Wong, H. W., Miake-Lye, R. C., Beyersdorf, A. J., Anderson,
1029 B. E., Thornhill, K. L., Winstead, E. L., Corporan, E., Dewitt, M. J., Klingshirn, C. D., Wey, C.,
1030 Tacina, K., Liscinsky, D. S., Howard, R. and Bhargava, A.: Particulate emissions of gas
1031 turbine engine combustion of a fischer-tropsch synthetic fuel, *Energy Fuels*, 24(11), 5883–
1032 5896, doi:10.1021/ef100727t, 2010.
- 1033 Timko, M. T., Fortner, E., Franklin, J., Yu, Z., Wong, H. W., Onasch, T. B., Miake-Lye, R. C. and
1034 Herndon, S. C.: Atmospheric measurements of the physical evolution of aircraft exhaust
1035 plumes, *Environ. Sci. Technol.*, 47(7), 3513–3520, doi:10.1021/es304349c, 2013.
- 1036 Trueblood, M. B., Lobo, P., Hagen, D. E., Achterberg, S. C., Liu, W. and Whitefield, P. D.:
1037 Application of a hygroscopicity tandem differential mobility analyzer for characterizing
1038 PM emissions in exhaust plumes from an aircraft engine burning conventional and
1039 alternative fuels, *Atmos. Chem. Phys.*, 18(23), doi:10.5194/acp-18-17029-2018, 2018.
- 1040 Ugarte, D.: Curling and closure of graphitic networks under electron-beam irradiation,
1041 *Nature*, 359(6397), 707–709, doi:10.1038/359707a0, 1992.
- 1042 Virkkula, A.: Erratum: Calibration of the 3-wavelength particle soot absorption



- 1043 photometer (3λ PSAP) (Aerosol Science and Technology (2002) 39 (68-83)), Aerosol Sci.
1044 Technol., 44(8), 706–712, doi:10.1080/02786826.2010.482110, 2010.
- 1045 Vozka, P., Vrtiška, D., Šimáček, P. and Kilaz, G.: Impact of Alternative Fuel Blending
1046 Components on Fuel Composition and Properties in Blends with Jet A, Energy Fuels, 33(4),
1047 3275–3289, doi:10.1021/acs.energyfuels.9b00105, 2019.
- 1048 Vander Wal, R. L. and Choi, M. Y.: Pulsed laser heating of soot: morphological changes,
1049 Carbon N. Y., 37(2), 231–239, doi:10.1016/S0008-6223(98)00169-9, 1999.
- 1050 Vander Wal, R. L., Bryg, V. M. and Huang, C.-H.: Aircraft engine particulate matter: Macro-
1051 micro- and nanostructure by HRTEM and chemistry by XPS, Combust. Flame, 161(2), 602–
1052 611, doi:10.1016/j.combustflame.2013.09.003, 2014.
- 1053 Williams, P. I., Allan, J. D., Lobo, P., Coe, H., Christie, S., Wilson, C., Hagen, D., Whitefield, P.,
1054 Raper, D. and Rye, L.: Impact of alternative fuels on emissions characteristics of a gas
1055 turbine engine - Part 2: Volatile and semivolatile particulate matter emissions, Environ.
1056 Sci. Technol., 46(19), doi:10.1021/es301899s, 2012.
- 1057 Wilson, G. R., Edwards, T., Corporan, E. and Freerks, R. L.: Certification of alternative
1058 aviation fuels and blend components, Energy Fuels, 27(2), 962–966,
1059 doi:10.1021/ef301888b, 2013.



1060 7 Figures and Tables

1061 Table 1. Properties of the fuels used for the ground-based measurements (fuel
1062 samples acquired from wing-tank after test).

Property	Method	JP-8	REF3	REF4	SAF1	SAF2	SAF3
Aromatics [vol%]	ASTM D1319	19.9	18.6	16.5	9.6	10.8	15.2
Hydrogen H [mass%]	ASTM D7171	13.86	13.65	14.08	14.40	14.51	14.04
Sulphur, total [ppm]	ISO 20884	1240	105	5.7	56.8	4.1	58.6
Naphthalenes [mass%]	ASTM D1840	1.49	1.17	0.13	0.61	0.05	0.64
Smoke point [mm]	ASTM D1322	23.0	23.0	27.0	30.0	30.0	28.0

1063



Table 2. Instruments used to measure nvPM and key measured properties. All instruments reported data at 1 second intervals except the SMPSs (45 second intervals for NRC and DLR; 60 seconds for NASA) and filter samplers. Instrument abbreviations are defined in the text.

Operator	Instrument	Acronym	Species measured	Sampling duration [s]	Units	Penetration functions ^d
NASA	Particle soot absorption photometer	PSAP	nvPM ^a mass	1	$\mu\text{g m}^{-3}$	1
	Tricolor absorption photometer	TAP	nvPM ^a mass	1	$\mu\text{g m}^{-3}$	1
	Scanning mobility particle sizer	SMPS	Total PSD (10 to 278 nm)	45	particles cm^{-3} , and $\mu\text{g m}^{-3}$	1
	Thermo-denuder with SMPS	TD-SMPS	nvPM PSD ^b (10 to 278 nm)	45	$\mu\text{g m}^{-3}$	1, 4
NRC	CO ₂ sensor	LI-COR 7000	CO ₂	1	ppmv	-
	Cavity-attenuated phase shift PM _{SSA} monitor (660 nm)	CAPS (NRC)	nvPM ^a mass	1	$\mu\text{g m}^{-3}$	1
	Photoacoustic extinctionmeter	PAX	nvPM ^a mass	1	$\mu\text{g m}^{-3}$	1
	Laser-induced-incandescence	LII-300 (NRC; 2x)	nvPM ^b mass	1	$\mu\text{g m}^{-3}$	1
	Catalytic stripper SMPS	CS-SMPS	nvPM PSD (8.6 to 278 nm)	45	particles cm^{-3}	1, 3
MST (NARS)	AVL Particle Counter Advanced	APC	nvPM number	1	particles cm^{-3}	1, 2
	Micro Soot Sensor	MSS Plus	nvPM ^a mass	1	$\mu\text{g m}^{-3}$	1, 2
	Laser-induced-incandescence	LII-300 (NARS)	nvPM ^c mass	1	$\mu\text{g m}^{-3}$	1, 2
	CO ₂ sensor	LI-COR 840A	CO ₂	1	ppm	-
	Differential mobility spectrometer	DMS500	Total PSD (5 to 1000 nm)	1	particles cm^{-3}	1, 2
ARI	Cavity-attenuated phase shift PM _{SSA} monitor (630 nm)	CAPS (ARI)	nvPM ^a mass	1	$\mu\text{g m}^{-3}$	1, 2

^anvPM measured via particulate absorption as equivalent BC (eBC). ^bParticle size distribution, here measured with respect to mobility diameter. ^cnvPM measured via laser-induced incandescence as refractory BC (rBC). ^dNumbers are indices corresponding to the penetration functions shown in Figure 4.

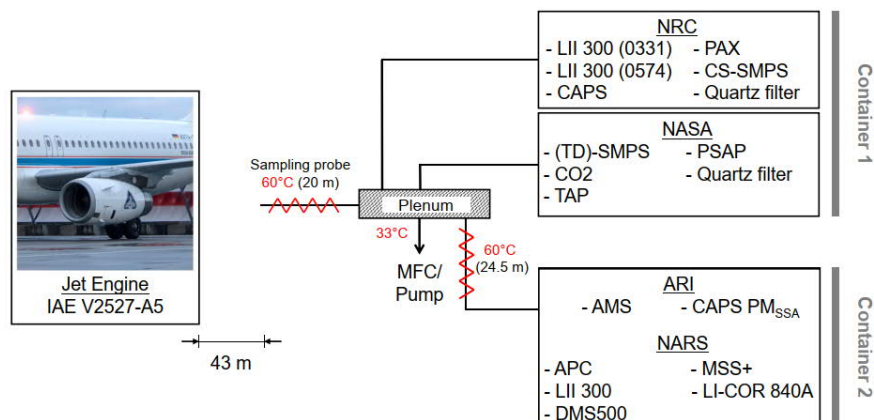


1068 Table 3. Summary of the ratios between the EI_m of individual instruments and the
 1069 geometric mean of the Group 1 (real time) instruments. The corresponding raw
 1070 data are shown in Figure 11. Regression: linear regression against Group 1
 1071 geometric mean weighted by standard deviations, with $k = 2$ uncertainties from fit.
 1072 SD: standard deviation. RSD: Relative SD. Group 1: real time instruments. Group 2:
 1073 integrative instruments.

1074

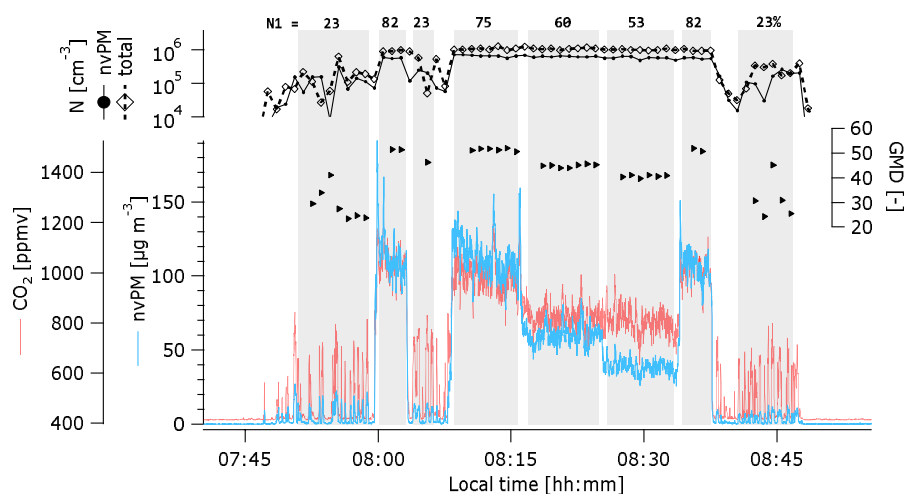
Group	Instrument	EI_{mass} Ratio vs. Group 1			Regression vs. Group 1	
		Mean	SD	RSD [%]	Intercept	Slope
1	CAPS PM_{SSA} (ARI)	0.84	0.08	10	12 ± 19	0.8 ± 0.1
1	CAPS PM_{SSA} (NRC)	0.99	0.09	9	-0.3 ± 0.8	1.01 ± 0.04
1	LII (NARS)	1.24	0.18	15	27 ± 6	1.03 ± 0.04
1	LII (NRC-0331)	1.07	0.1	9	-15 ± 42	1.17 ± 0.16
1	LII (NRC-0574)	0.78	0.08	10	-17.1 ± 2	0.88 ± 0.08
1	MSS+	1.07	0.14	13	17.8 ± 5	0.92 ± 0.04
1	PAX	1.06	0.18	17	-15 ± 1	1.21 ± 0.02
2	CS-SMPS	1.50	0.27	18	12 ± 22	1.02 ± 0.12
2	TD-SMPS	1.14	0.26	23	-5 ± 1	1.47 ± 0.04
2	PSAP	0.89	0.32	36	8 ± 16	0.82 ± 0.08
2	TAP	0.88	0.12	14	6 ± 6	0.75 ± 0.02

1075



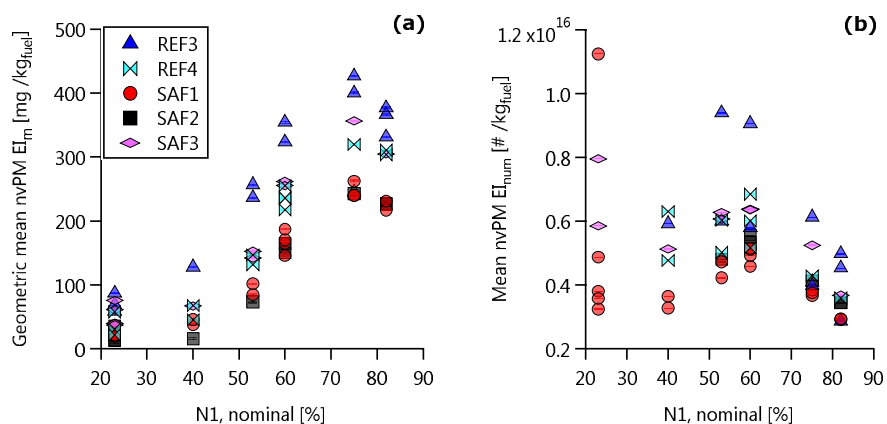
1076

1077 Figure 1. Schematic of sampling configuration behind the DLR ATRA aircraft. The length
 1078 and flow rate of sampling lines from the manifold to the various instruments varied as
 1079 described in the text. The NRC and NASA instruments were all placed within Container 1,
 1080 while the NARS and ARI instruments were placed in Container 2. For simplicity, the figure
 1081 omits a short heated line connecting the first plenum to the NARS. The ARI instruments
 1082 were downstream of all NARS instruments except the DMS500 (see Lobo et al., 2016 for
 1083 detailed NARS diagram). NARS = North American Reference System.



1084

1085 Figure 2. Illustration of a typical test run. Variation in the CO₂ concentration was not due
 1086 to instrument noise, as illustrated by the CO₂ measurements prior to and following
 1087 sampling. A representative nvPM mass instrument is shown by the blue trace. Sizing
 1088 information (GMD) is shown by the black symbols (triangles: GMD; diamonds with dashed
 1089 line: total PM number; spheres with solid line: nvPM number measured with the CS-
 1090 SMPS).

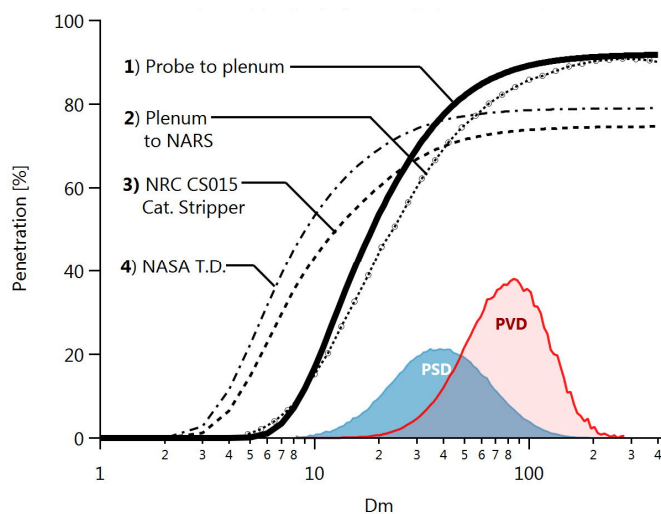


1091

1092

1093 Figure 3. Relationship between nvPM (a) EI_m and (b) EI_{num} with N1 for all data obtained
 1094 with the V2527-A5 engine. The trends shown in this plot are discussed further in the
 1095 companion article (Schripp and NDMAX-Team, 2021). The ordinate values are the
 1096 geometric mean discussed in the text.

1097



1098

1099 Figure 4. Penetration functions for the main probe-to-plenum sampling line as well as
 1100 other components in the sampling system. Shaded areas illustrate a representative
 1101 particle size (PSD) and volume (PVD) distribution measurement with GMD 34 nm and GSD
 1102 1.72. PSD data for all test points and instruments are provided in the supplement. NARS:
 1103 North American Reference System; CS015: Catalytic Stripper; T.D.: thermodenuder.

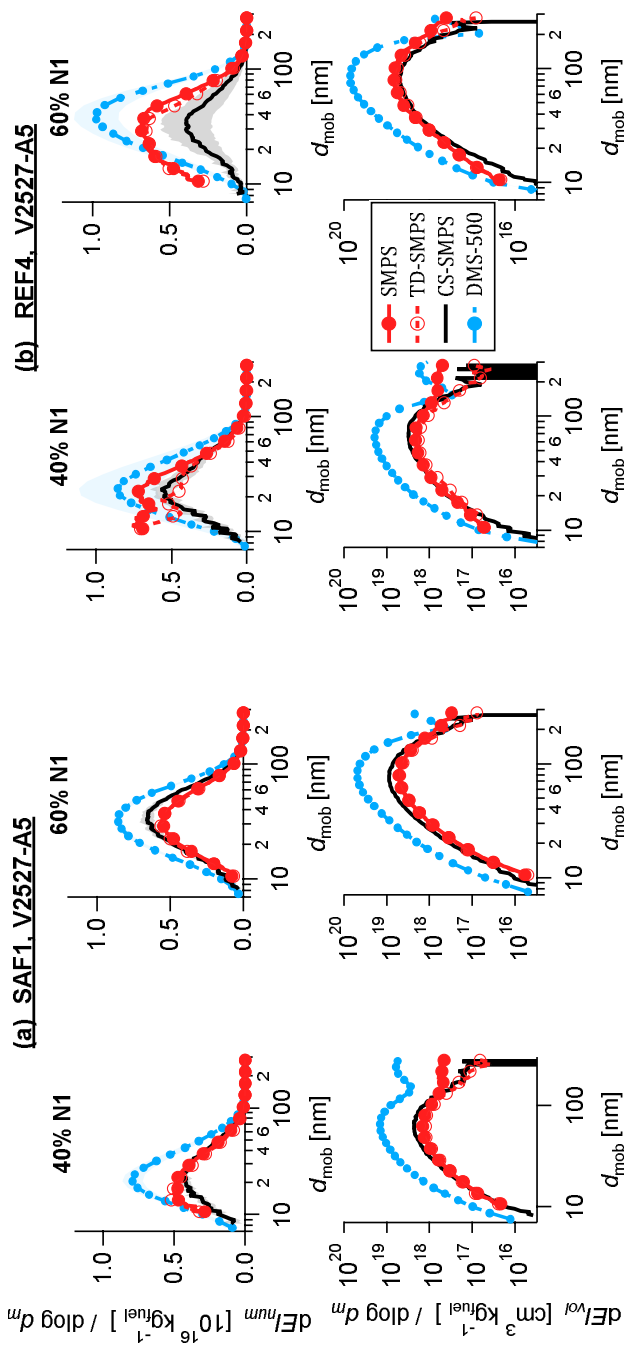


Figure 5. Selected PSDs illustrating the V2527-A5 engine with (a) SAF1 fuel and (b) REF4 fuel. Each panel shows 60% N1 on the right and a lower N1 on the left: 40% for (a), 60% for (b). Note that the TD-SMPS and CS-SMPS (red open circles and black line) represent nvPM, while the SMPS and DMS500 represent vPM.

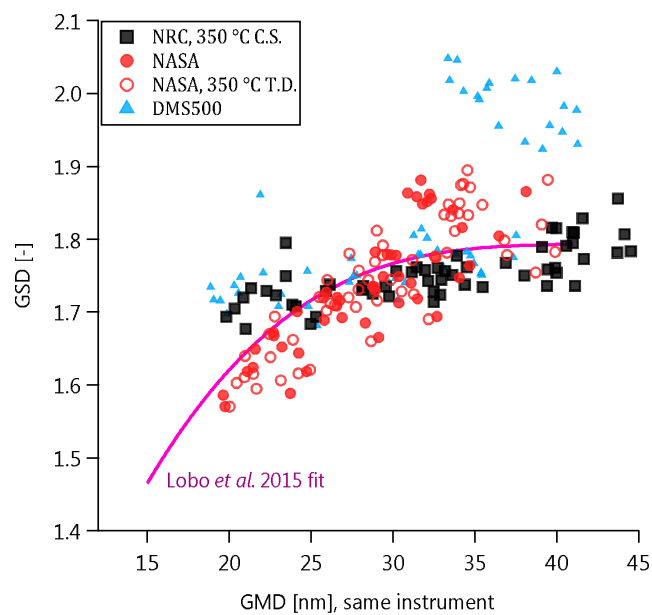
11104

11105

11106

11107

11108



1109

1110 Figure 6. GSD versus GMD data as by measured by each particle sizer for all test points.

1111 Higher GSDs for the DMS500 correspond to bimodal PSDs (non-volatile and volatile
1112 modes). Note that size-dependent particle losses (see penetration functions in Figure 4)
1113 may affect both GSD and GMD. Based on Figure 12, the TD-SMPS (NASA) data may be more
1114 accurate than the CS-SMPS data (see text). Fit is from Lobo et al. (2015c).

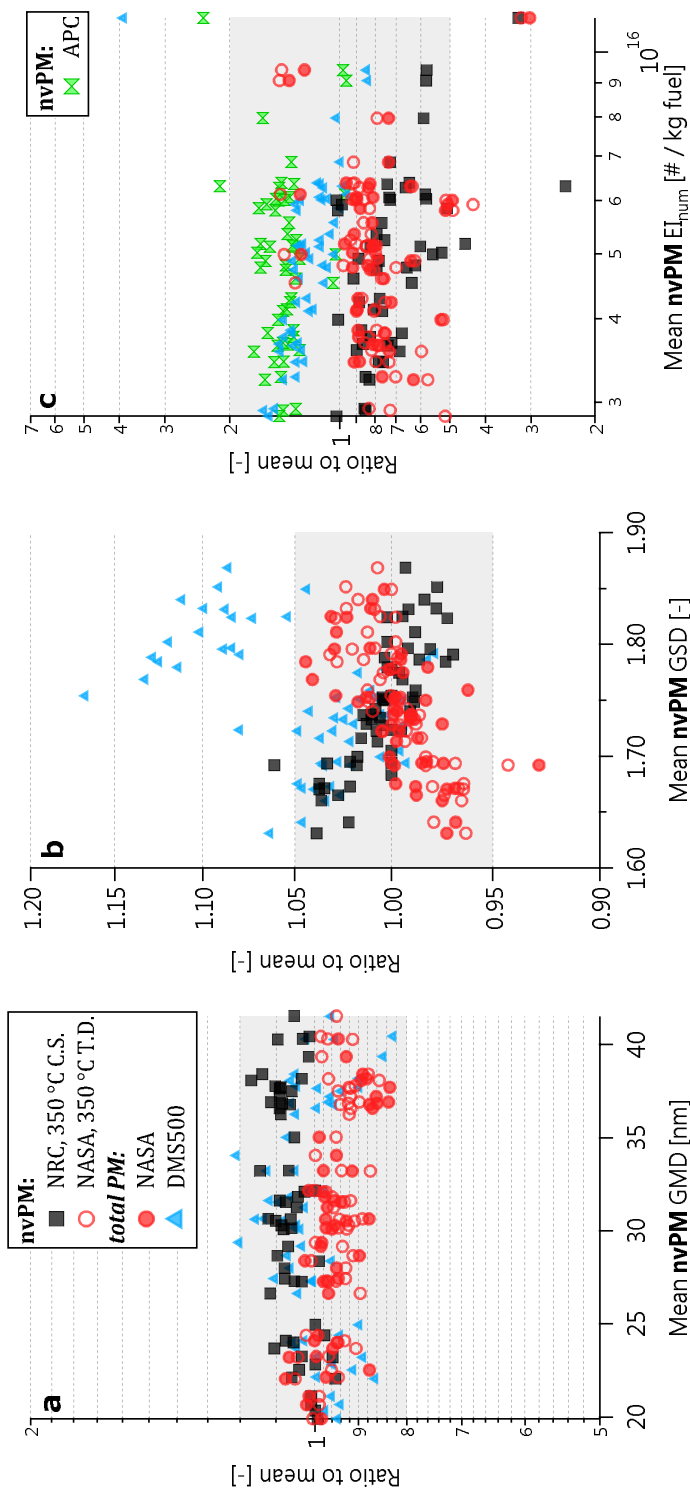


Figure 7. Comparison of size and number measurements in terms of GMD, GSD, and E_{h} . Grey shading shows 20%, 5%, and 200% in GMD, GSD, and E_{h} , respectively. In panels (a) and (b), mean is defined from the CS-SMPS (NRC) and TD-SMPS (NASA) data. In panel (c), the mean additionally includes the APC (NARS) data (the APC is in the NARS and uses a TSI 3790E CPC).

11115
 11116
 11117
 11118
 11119

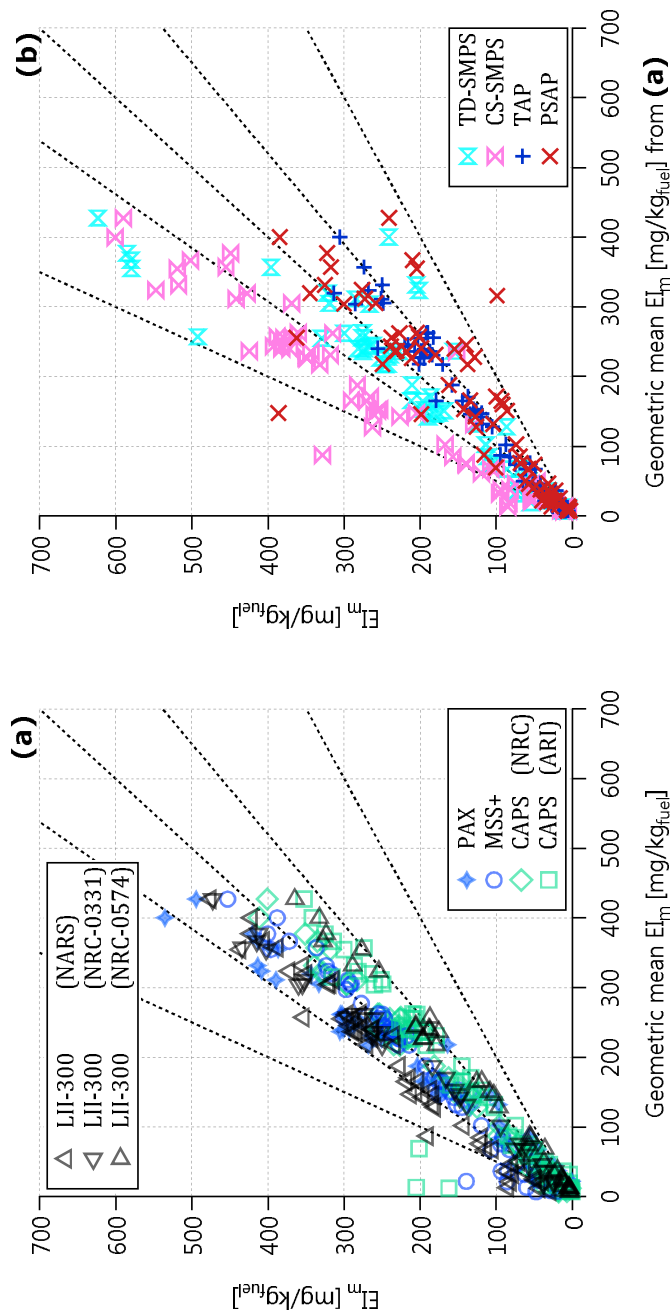


Figure 8. E_{I_m} scatterplot for (a) real-time and (b) integrative nvPM measurements. The term integrative refers to SMPS measurements (mass concentrations estimated by assuming unit-density spheres) and filter photometer measurements (mass concentrations estimated using standard empirical relationships between light attenuation and light absorption). The abscissa of both panels is the geometric mean of all available data from the 7 real-time sampling instruments plotted in (a). Angled lines illustrate slopes of 2, 2⁻¹, 1.3, 1.3⁻¹, and 1.0.

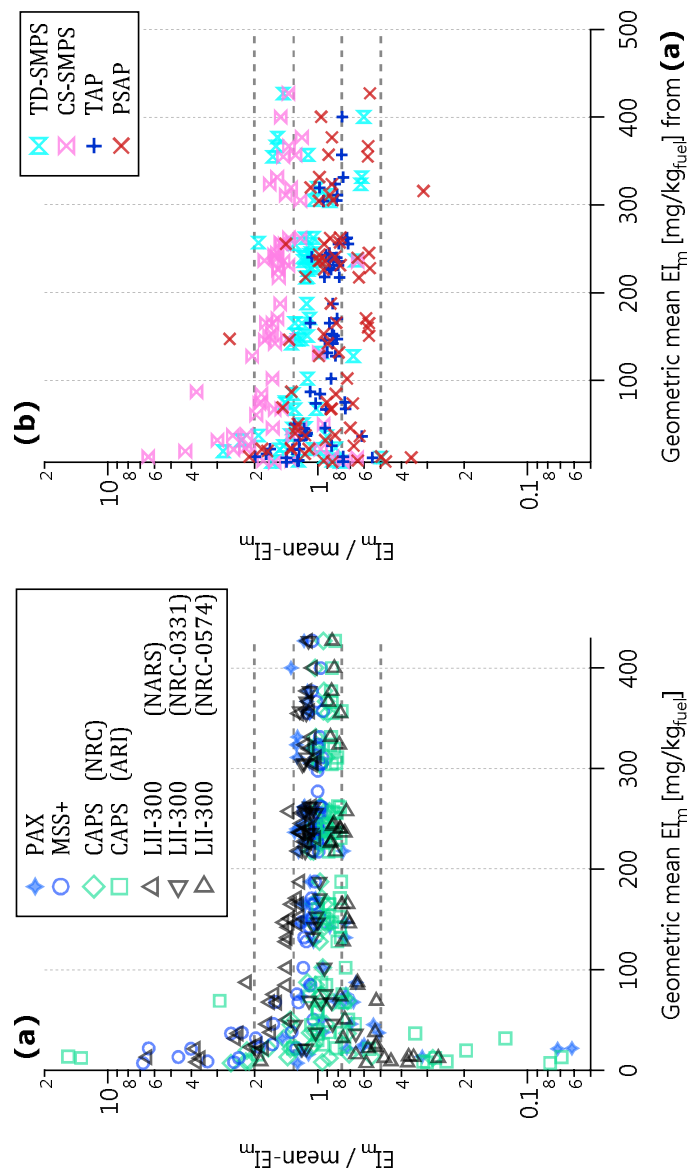
1120

1121

1122

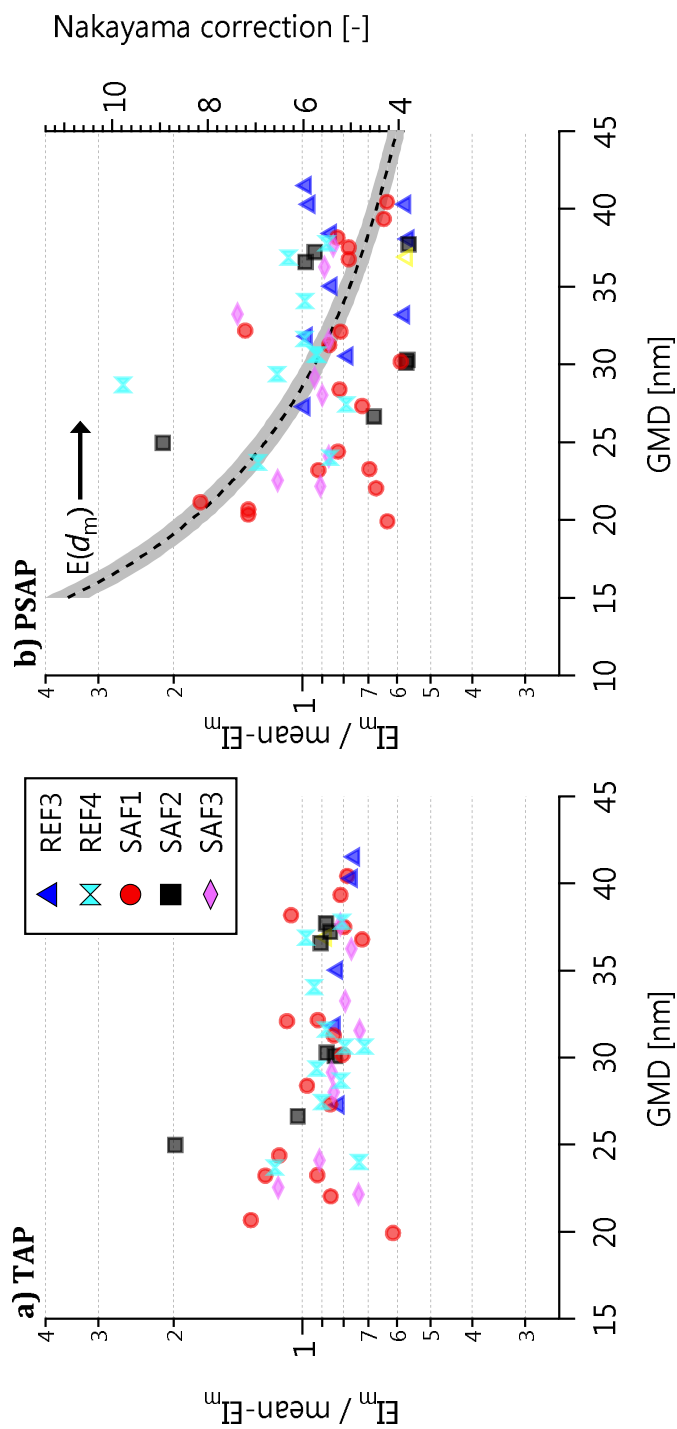
1123

1124



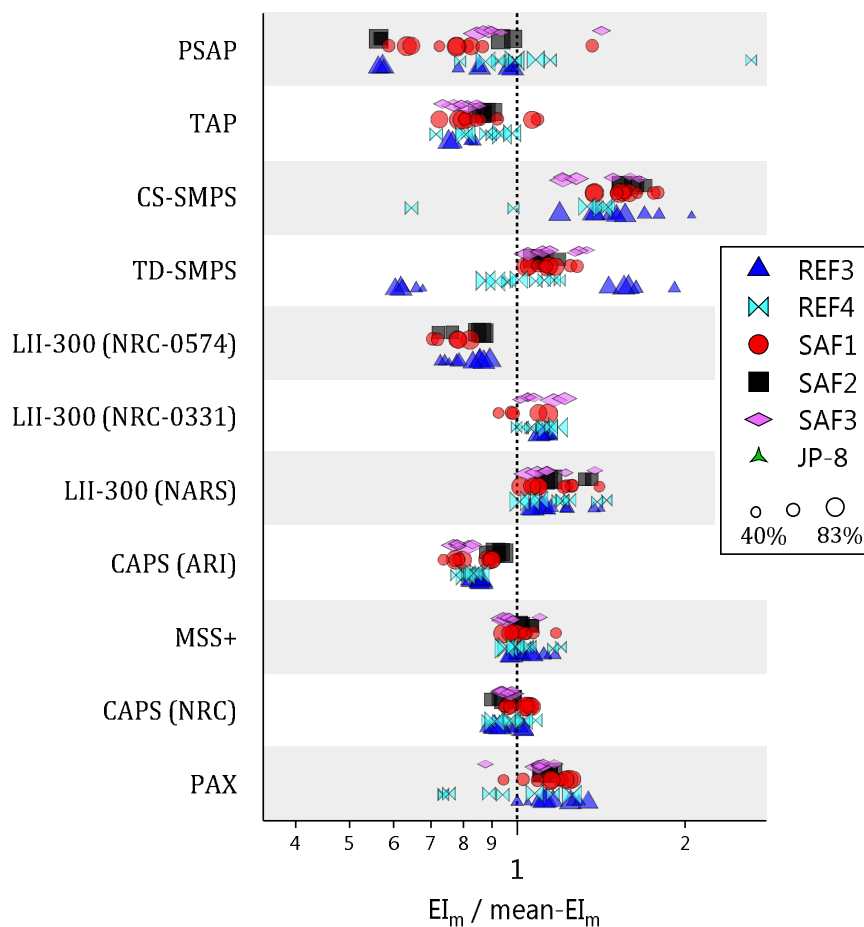
1125
 1126
 1127
 1128

Figure 9. Ratio plots corresponding to Figure 8. The inner and outer horizontal lines show ratios of 2, 2⁻¹, 1.3, 1.3⁻¹, and 1.0. Agreement between the instruments is poorer at $E_m < 100 \text{ mg/kg}_{\text{fuel}}$, which corresponds to an approximate concentration of $10 \mu\text{g m}^{-3}$ (the exact conversion factor varies with CO_2 concentration and fuel properties) and close to the limit of detection for most instruments.



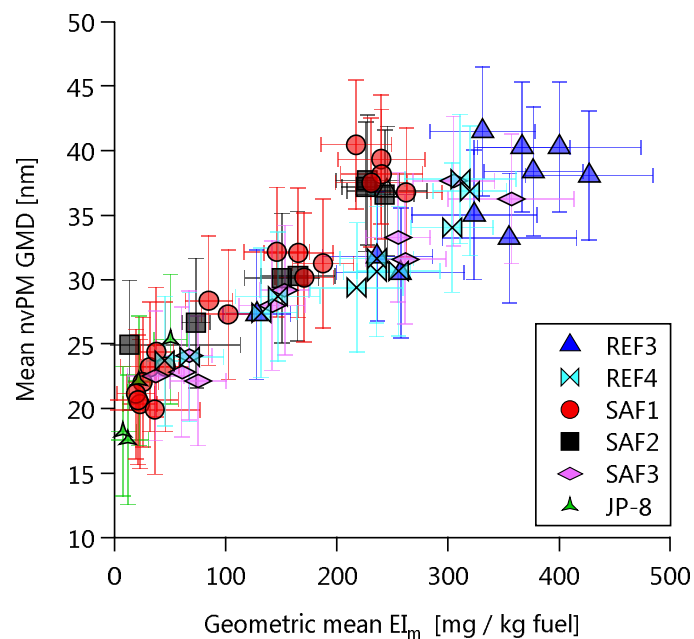
1129
 1130
 1131
 1132

Figure 10. $E_m / \text{mean-}E_m$ ratios from Figure 9 for the TAP and PSAP (the filter-based photometers) only, plotted as a function of geometric mean mobility diameter (GMD) to highlight potential size-dependent sensitivities of these instruments. The curve labelled $E(d_m)$ in b) plots the size-dependent PSAP correction factor given by Nakayama et al. (2010; Eq. 8) with 1σ uncertainties shaded.



1133

1134 Figure 11. Ratios of Figure 9 grouped by fuel. All fuels except JP-8 were combusted in the
 1135 V2527-A5 engine; JP-8 was combusted in the CFM56-2C1 engine. Shading is to guide the
 1136 eye. Symbols are sized by N1 thrust. Plot excludes data where $EI_m < 25 \text{ mg/kg}_{\text{fuel}}$ and N1
 1137 thrust below 40% to minimize the effects of instrument noise and wind speed,
 1138 respectively, on the ratios.

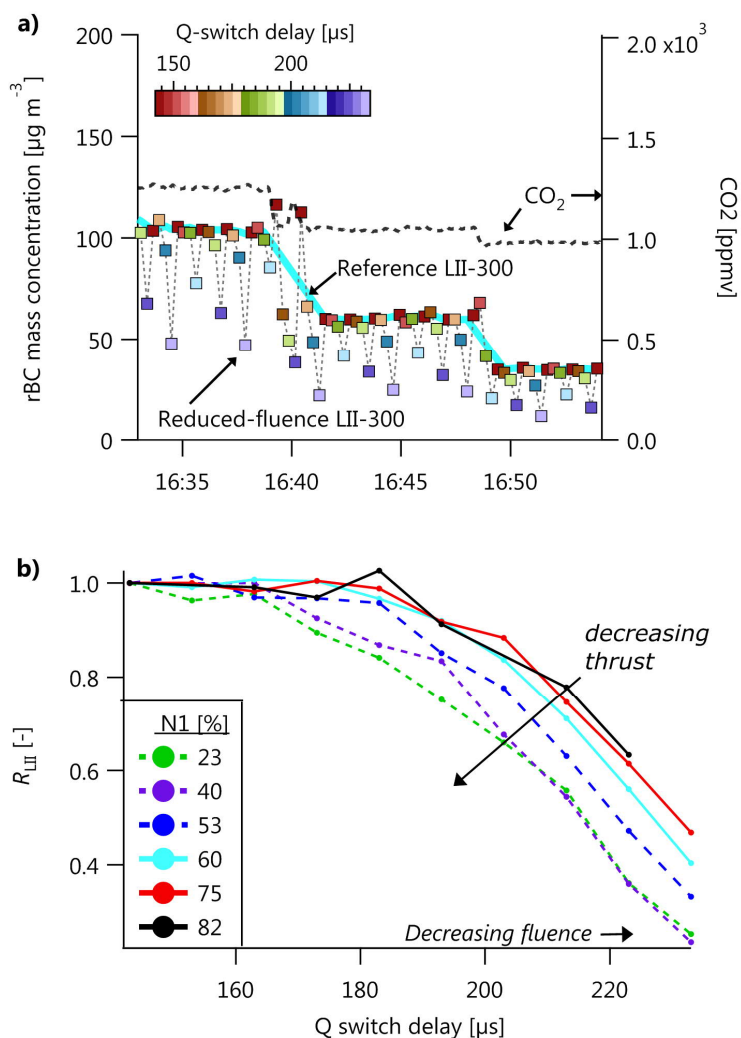


1139

1140 Figure 12. Scatterplot of the mean nvPM GMD within test points against geometric
1141 mean nvPM EI_m from Figure 8a. The correlation with GMD and EI_m indicates that Figure 9
1142 implicitly represented different particle sizes.

1143

1144



1145

1146 Figure 13. (a) LII 300 experiment time series, where one LII 300 was operated with
 1147 increased Q-switch delays to reduce its laser fluence (squares) and the other was operated
 1148 at standard fluence (solid line). CO_2 data are also shown for context. (b) The ratio R_{LII}
 1149 of the concentration reported by the reduced-fluence LII divided by the reference LII. It is
 1150 evident from (b) that the standard high-fluence conditions generate data that are
 1151 independent of N1 thrust, and that moderate- and low-fluence conditions (Q-switch delays
 1152 greater than about 165 to 185 μs) display a weak dependence on thrust.

1153